



저작자표시-비영리-변경금지 2.0 대한민국

이용자는 아래의 조건을 따르는 경우에 한하여 자유롭게

- 이 저작물을 복제, 배포, 전송, 전시, 공연 및 방송할 수 있습니다.

다음과 같은 조건을 따라야 합니다:



저작자표시. 귀하는 원저작자를 표시하여야 합니다.



비영리. 귀하는 이 저작물을 영리 목적으로 이용할 수 없습니다.



변경금지. 귀하는 이 저작물을 개작, 변형 또는 가공할 수 없습니다.

- 귀하는, 이 저작물의 재이용이나 배포의 경우, 이 저작물에 적용된 이용허락조건을 명확하게 나타내어야 합니다.
- 저작권자로부터 별도의 허가를 받으면 이러한 조건들은 적용되지 않습니다.

저작권법에 따른 이용자의 권리는 위의 내용에 의하여 영향을 받지 않습니다.

이것은 [이용허락규약\(Legal Code\)](#)을 이해하기 쉽게 요약한 것입니다.

[Disclaimer](#)

이학박사 학위논문

**Magnetic properties of van der Waals  
antiferromagnet probed by X-ray photoemission  
electron microscopy**

엑스선 광전자 현미경을 이용한 반데르발스  
반강자성체의 자성 연구

2023 년 8 월

서울대학교 대학원

물리천문학부 물리학전공

이 유 진

**Magnetic properties of van der Waals  
antiferromagnet probed by X-ray  
photoemission electron microscopy**

Youjin Lee

Supervised by  
Professor Je-Geun Park

A Dissertation submitted to the Faculty of Seoul National  
University in Partial Fulfillment of the Requirements for the  
Degree of Doctor of Philosophy  
August 2023

*Department of Physics and Astronomy  
Graduate School  
Seoul National University*

**Magnetic properties of van der Waals antiferromagnet  
probed by X-ray photoemission electron microscopy**

엑스선 광전자 현미경을 이용한 반데르발스 반강자성체의  
자성 연구

지도 교수 박 제 근

이 논문을 이학박사 학위논문으로 제출함  
2023 년 8 월

서울대학교 대학원  
물리천문학부  
이 유 진

이유진의 이학박사 학위논문을 인준함  
2023 년 6 월

위 원 장	<u>김 기 훈</u>	(인)
부위원장	<u>박 제 근</u>	(인)
위 원	<u>민 흥 기</u>	(인)
위 원	<u>김 도 현</u>	(인)
위 원	<u>Armin Kleibert</u>	(인)

## **Abstract**

The simple exfoliation of graphene from the bulk graphite using scotch tape opened a new phase of condensed matter in 2004. From the monumental demonstration, a flush of studies on 2D van der Waals (vdW) materials followed, and eventually, the first 2D vdW antiferromagnetic monolayer was experimentally demonstrated in 2016. 2D vdW magnets are the ideal platform for studying 2D magnetism. Different spin Hamiltonian models in diverse vdW magnets provide the experimental testbed for a theory of 2D magnetism. The research field on vdW 2D magnet has expanded from the intrinsic magnetic property on the pristine material to heterostructure and even the moiré structure.

As the research area has expanded rapidly, the proper probing techniques are essential for the vdW magnet study. Despite their physical significance and promising applications, determining the magnetic state of ultrathin vdW magnets, especially the antiferromagnetic order, remains an ongoing challenge. The small volume of exfoliated vdW material poses the first obstacle to detection, and the zero net magnetization in antiferromagnets presents an additional hurdle.

To expand the measurement technique and find the emergent phenomena in the 2D limit, I applied X-ray photoemission microscopy (X-PEEM) with linearly polarized X-rays to investigate the 2D vdW antiferromagnet. X-ray magnetic linear dichroism can detect the antiferromagnetic order from the optical dipole selection rule. The high spatial resolution of X-PEEM enables us to measure the exfoliated few-layer vdW antiferromagnet

with lateral dimensions on the order of a few micrometers.

In my study, I focused on examining the magnetic properties of two different spin Hamiltonian vdW antiferromagnets: Ising type FePS<sub>3</sub> and anisotropic Heisenberg type NiPS<sub>3</sub>. I confirmed that the long-range antiferromagnetic order persisted down to monolayer FePS<sub>3</sub> as Onsager theoretically expected in the 1960s. Furthermore, I quantified the magnetic anisotropy of FePS<sub>3</sub> as a function of thickness by analyzing observed X-ray absorption spectra and conducting multiplet calculations. Bulk FePS<sub>3</sub> possessed large magnetic anisotropy stemming from the unquenched orbital moment and spin-orbit coupling. Additionally, the thickness dependence on magnetic anisotropy provided the insight into the substrate effect, a factor often overlooked in vdW materials research. In the case of exfoliated NiPS<sub>3</sub>, I observed the antiferromagnetic domains. They showed the thermal fluctuations demonstrating the Néel vectors' mobility. I figured out that the formation and thermal fluctuation of domains originated from the small magnetic anisotropy of NiPS<sub>3</sub>.

**Keywords:** 2D van der Waals magnet, Antiferromagnetism, X-ray photoemission electron microscopy, X-ray magnetic linear dichroism

**Student Number:** 2016-20314

<b>Abstract</b> .....	<b>i</b>
<b>List of Tables</b> .....	<b>vi</b>
<b>List of Figures</b> .....	<b>vii</b>
<b>1 Introduction</b> .....	<b>1</b>
1.1 Two-dimensional magnetism .....	1
1.1.1 Novel phenomena in two-dimensional magnetic systems .....	2
1.2 Study of vdW antiferromagnet using XMLD- PEEM .....	3
1.3 Outline of thesis .....	6
<b>2 Theoretical background</b> .....	<b>11</b>
2.1 X-ray absorption and linear dichroism .....	11
2.1.1 X-ray absorption .....	11
2.1.2 Magnetic dichroism in X-ray absorption .....	13
2.1.3 Multiplet calculation .....	16
2.2 Magnetic anisotropy .....	22
2.3 Antiferromagnetic domain .....	23
<b>3 Experimental techniques</b> .....	<b>28</b>
3.1 X-ray photoemission microscopy (XPEEM) in SIM beamline .....	28
3.1.1 Synchrotron radiation .....	28
3.1.2 XPEEM equipment and experiment .....	29
3.2 Sample preparation .....	32
3.2.1 Lithography of the gold marker .....	32
3.2.2 Exfoliation of a single crystal .....	32

3.2.3	Optimal substrate for charging issues .....	33
<b>4</b>	<b>Large magnetic anisotropy in the few-layer vdW antiferromagnet FePS<sub>3</sub> .....</b>	<b>36</b>
4.1	Introduction .....	36
4.2	Van der Waals Ising antiferromagnet FePS <sub>3</sub> .....	37
4.3	Methods .....	38
4.3.1	Sample preparation .....	38
4.3.2	XPEEM experiment .....	39
4.4	Results .....	40
4.4.1	X-ray absorption spectra .....	40
4.4.2	Magnetic anisotropy .....	46
4.4.3	XMLD asymmetric images .....	49
4.4.4	Thickness dependency .....	51
4.5	Summary .....	56
<b>5</b>	<b>Magnetic domains and their thermal fluctuations in vdW antiferromagnet NiPS<sub>3</sub> .....</b>	<b>60</b>
5.1	Introduction .....	60
5.1.1	Magnetic domains in TMPS <sub>3</sub> .....	60
5.1.2	vdW antiferromagnet NiPS <sub>3</sub> .....	62
5.2	Method .....	63
5.3	Results .....	63
5.3.1	Observation of magnetic domain .....	63
5.3.2	Temperature dependence of magnetic domain .....	65
5.3.3	Determination of Néel vector axis.....	67

5.3.4 Thermal fluctuation of magnetic domain .....	71
5.4 Summary .....	74
<b>6 Summary and Outlook .....</b>	<b>77</b>
6.1 Summary .....	77
6.2 Outlook .....	77
<b>Publication lists .....</b>	<b>81</b>
<b>Abstract in Korean (국문 초록) .....</b>	<b>84</b>
<b>Acknowledgement (감사의 글) .....</b>	<b>87</b>

## **List of Tables**

2.1 Expressions of X-ray absorption coefficients $A_{JJ'}^q$ .....	14
4.1 Summary of parameters used for the multiplet simulation .....	44
4.2 Modified parameters for monolayer's multiplet simulation .....	54
5.1 Summary of parameters for multiplet simulation .....	69

## List of Figures

1.1	Optical and electronic probes of few-layer vdW AFM .....	5
2.1	Energy and wavelength of electromagnetic spectrum .....	11
2.2	X-ray absorption process for 3d transition metal atom .....	12
2.3	Ni $L_{2,3}$ -edge X-ray absorption spectra of NiO with/without crystal and exchange fields .....	23
3.1	PEEM setup in SIM beamline in SLS .....	29
3.2	Schematic image of XPEEM in the SIM beamline .....	30
3.3	Extraction of XA spectrum of the ROI from the successive XPEEM images .....	31
3.4	Exfoliation of van der Waals single crystal .....	33
3.5	OM and XPEEM images of exfoliated NiPS <sub>3</sub> on an ITO/Si substrate and a SiO <sub>2</sub> substrate with the gold window .....	34
3.6	XA spectra of Ni $L_{2,3}$ -edge from bulk, 2L on the ITO/Si substrate, and 2L NiPS <sub>3</sub> on the SiO <sub>2</sub> substrate with the gold window .....	35
4.1	Ising-type vdW antiferromagnet FePS <sub>3</sub> .....	38
4.2	FePS <sub>3</sub> sample and X-PEEM experiment .....	39
4.3	Temperature-dependent XA spectra .....	41
4.4	Exchange field effect on the multiplet simulation .....	42
4.5	Reproduction of XMLD spectra at 65 K with the long-range magnetic order in the multiplet calculation .....	43

*List of Figures*

---

4.6	Magnetic anisotropies from the MC simulation .....	46
4.7	Trigonal elongation and corresponding orbital splitting in FePS <sub>3</sub> .....	48
4.8	XMLD asymmetric map .....	49
4.9	Normalised XMLD contrast value A from the XMLD asymmetric map .....	50
4.10	Thickness-dependent XA and XMLD spectra .....	51
4.11	Temperature-dependent $\langle M_z^2 \rangle - \langle M_x^2 \rangle$ and X <sub>M</sub> in few-layer FePS <sub>3</sub> .....	52
4.12	Magnetic anisotropy as a function of thickness extracted from MC simulation and Bruno's model .....	53
4.13	Substrate effect on the 1 L .....	54
4.14	Raman shift in few-layer FePS <sub>3</sub> .....	56
5.1	Observation of antiferromagnetic domains in TMPS <sub>3</sub> via optical techniques ...	61
5.2	Magnetic structure and magnetic susceptibility of NiPS <sub>3</sub> .....	62
5.3	Magnetic domains in NiPS <sub>3</sub> .....	64
5.4	Temperature dependence on the magnetic domains .....	65
5.5	Polarisation-dependent Raman experiment for determining in-plane crystalline axis .....	67
5.6	XA and X(M)LD spectra at Ni L <sub>3</sub> edge .....	68
5.7	Determination of Néel vector axes in domains at 70 K .....	70
5.8	XMLD asymmetric images showing domains with thermal fluctuation .....	71
5.9	Reproduced XMLD map for magnetic domains in NiPS <sub>3</sub> via MC simulation ...	73
5.10	Antiferromagnetic domains in another NiPS <sub>3</sub> flake .....	74

## **Chapter 1. Introduction**

### **1.1 Two-dimensional van der Waals magnet**

Van der Waals (vdW) materials are characterized by their layered structures and relatively weak interlayer interactions. This property allows for the straightforward creation of two-dimensional (2D) magnets using adhesive tape and a single crystal of a vdW magnet, as first demonstrated with graphene. Before the realisation of 2D magnets from the exfoliation of vdW magnet, there have been attempts for the experimental achievement of the 2D magnetic system. The anisotropic exchange interaction, large intralayer coupling compared to the interlayer coupling, can be found in the quasi-2D bulk magnet such as  $\text{K}_2\text{NiF}_4$  [Ref. 1.1]. The monolayer epitaxial ferromagnetic film [Ref. 1.2] and dilute magnetism in graphene [Ref. 1.3,1.4] achieved the coincident 2D spin and space dimensionality. Eventually, the magnetic vdW monolayer  $\text{FePS}_3$  was demonstrated in 2016 [Ref. 1.5]. The vdW magnet's merits over other 2D magnetic systems are the emerging physical phenomenon in the hetero- or homo-structures. Their intrinsic magnetism and weak interlayer coupling allow the diverse recombination with new functionality.

Theoretical foundations, such as Onsager's solution for the Ising system [Ref. 1.6], the Mermin-Wagner theorem [Ref. 1.7], and the Berezinskii–Kosterlitz–Thouless (BKT) transition in the XY model [Ref. 1.8], have predicted the 2D magnetism about 50 years before the first demonstration of 2D vdW magnet [Ref. 1.9]. These theories emphasize the

importance of magnetic anisotropy in 2D magnetic systems. In such systems, enhanced thermal fluctuations disrupt continuous rotational symmetries and short-range magnetic order. However, magnetic anisotropy can stabilize long-range magnetic order by opening a magnon excitation gap that counteracts the thermal agitation of magnons.

In contrast to the isotropic exchange interactions commonly found in three-dimensional (3D) magnets, van der Waals magnets exhibit highly anisotropic exchange interactions, with a significantly stronger in-plane exchange coupling compared to the out-of-plane component. The spin Hamiltonians, which describe the anisotropic exchange interactions, can vary widely among vdW magnets. For example, isostructural materials with different magnetic cations or non-magnetic anions can exhibit distinct magnetic anisotropies and be characterized by different spin Hamiltonians.

### **1.1.1 Transition metal thiophosphates $\text{TMPS}_3$**

Transition metal thiophosphates ( $\text{TMPS}_3$ ) with magnetic atoms (TM = Mn, Fe, and Ni) are isostructural insulators featuring a two-dimensional honeycomb magnetic lattice. Each compound is described by a distinct spin Hamiltonian:  $\text{MnPS}_3$  by an isotropic Heisenberg model [Ref. 1.10],  $\text{FePS}_3$  by an Ising system [Ref. 1.11,1.12], and  $\text{NiPS}_3$  by an anisotropic Heisenberg Hamiltonian [Ref. 1.13,1.14,1.15,1.16]. The differences in magnetic anisotropies result from a combination of orbital momentum from trigonal distortion on  $\text{TMS}_6$  octahedra and spin-orbit coupling [Ref. 1.17].

Theoretical predictions regarding these different 2D spin models were confirmed through thickness-dependent experiments on the magnetic order of  $\text{TMPS}_3$ . The substantial

perpendicular magnetic anisotropy in FePS<sub>3</sub> preserved its long-range magnetic order down to a monolayer [Ref. 1.9]. Consistent with the predictions of the Mermin-Wagner theorem, MnPS<sub>3</sub> and NiPS<sub>3</sub> lost their long-range magnetic order at the monolayer level [Ref. 1.18,1.19,1.20].

## **1.2 Study of vdW antiferromagnet using XMLD-PEEM**

Studying the magnetic state of atomically thin vdW antiferromagnets (AFMs) poses significant challenges due to their small volume ( $\sim 0.1 \text{ mm}^3$  for an exfoliated vdW flake) and the minuscule magnetic signal of AFMs. While neutron scattering and superconducting quantum interference device (SQUID) magnetometers successfully measure the magnetic properties of bulk AFMs, they are unsuitable for atomic-scale thin samples, as they require a larger volume to detect the magnetic signal. Consequently, extensive efforts have been made to utilize optical and electrical probes to investigate the magnetic properties of vdW AFMs in the monolayer limit.

Optical probes such as Raman spectroscopy and second harmonic generation (SHG) have been employed to detect magnetic order in ultrathin vdW AFMs. Raman spectroscopy can identify quasiparticle excitations, such as phonons and magnons [Ref. 1.9,1.20,1.21]. [Ref. 1.9] demonstrated that long-range magnetic order led to symmetry breaking, resulting in Raman peak splitting of the phonon mode. SHG is also sensitive to symmetry breaking caused by magnetic order [Ref. 1.19,1.22,1.23]. However, these techniques require strong spin-phonon coupling and specific symmetry conditions to detect the magnetic signal. For instance, inversion-broken Néel-type AFM MnPS<sub>3</sub> exhibits a

substantial SHG signal, while inversion-symmetric zigzag-type AFM FePS<sub>3</sub> and NiPS<sub>3</sub> display negligible SHG intensities [Ref. 1.22].

Electrical probes have been employed to study few-layer vdW AFMs, despite most of these materials being insulators or semiconductors. Researchers have fabricated graphene/few-layer insulating AFM/graphene structures and measured tunnelling magnetoresistance (TMR), which is dependent on the magnetic state of the insulating AFM [Ref. 1.24,1.25,1.26]. Other approaches include magneto-transport and magnon transport with heavy metals. By utilizing the spin Hall and inverse spin Hall effects with heavy metals, it is possible to measure magnetoresistance and magnon signals of few-layer vdW AFMs [Ref. 1.27,1.28]. However, these electrical methods indirectly assess the magnetic state and often involve complex fabrication processes.

In this study, we demonstrated that X-ray photoemission electron microscopy (XPEEM) with linearly polarised X-rays is an effective tool for detecting 2D vdW AFMs. XPEEM offers high spatial resolution on the order of tens of nanometres, enabling the probing of magnetic signals in exfoliated vdW AFMs and capturing nanometre-sized spin textures. Additionally, XPEEM exhibits high sensitivity to antiferromagnetic order. X-ray absorption intensities depend on the multiplet structure of the ground and excited states [Ref. 1.29,1.30], allowing for the investigation of local electronic and magnetic structures. The intensities vary based on the incident X-ray polarization due to the dipole selection rule [Ref. 1.31,1.32]. In particular, X-ray linear polarization dependence on magnetic order (X-ray magnetic linear dichroism, XMLD) is sensitive to the expectation value of the square local magnetic moment  $\langle M^2 \rangle$  [Ref. 1.31,1.33]. Consequently, XMLD-PEEM can

be applied to study ferromagnets, ferrimagnets, and even AFMs.

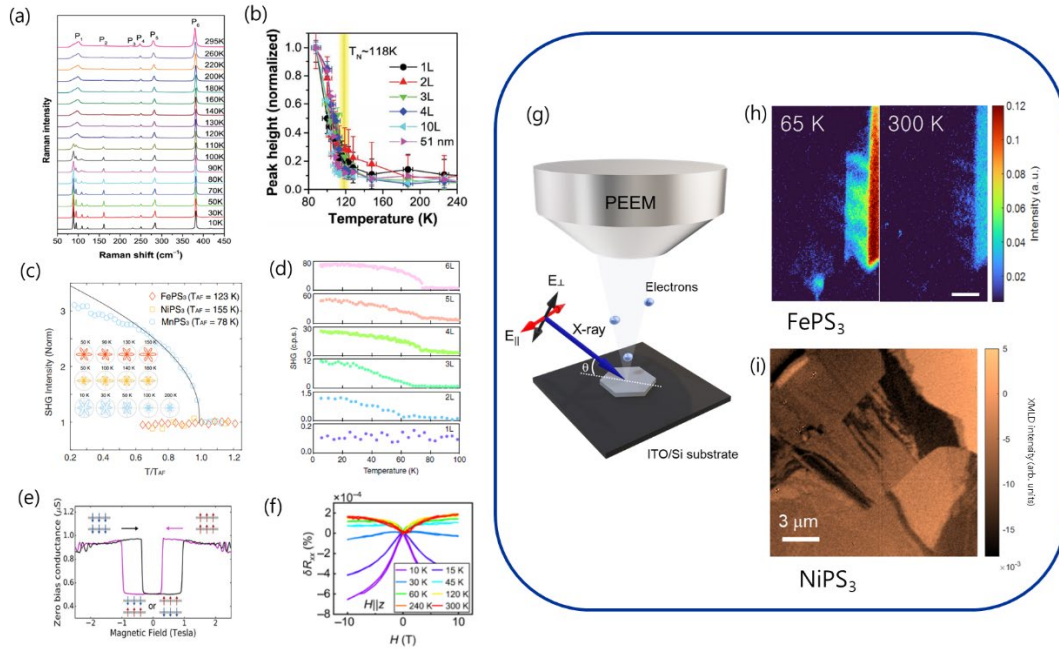


**Figure 1. Optical and electronic probes of few-layer vdW AFM.** (a–b) Raman experiments on FePS<sub>3</sub> [Ref. 1.5]: (a) Temperature dependence and (b) thickness dependence of FePS<sub>3</sub> Raman signals. (c–d) SHG experiments on TMPS<sub>3</sub>: (c) Temperature-dependent SHG signal in bulk TMPS<sub>3</sub> [Ref. 1.22], and (d) thickness-dependent SHG in MnPS<sub>3</sub> [Ref. 1.19]. (e) TMR of bilayer AFM CrI<sub>3</sub> [Ref. 1.25]. (f) Spin Hall experiment on CrPS<sub>4</sub>/Pt heterostructure [Ref. 1.27]. (g–i) XMLD-PEEM experiments on FePS<sub>3</sub> and NiPS<sub>3</sub> in this thesis: (g) Schematic representation of an X-PEEM experiment with two linearly polarised X-rays, (h) temperature dependence of XMLD intensity in few-layer FePS<sub>3</sub>, and (i) spin texture (antiferromagnetic domain) in exfoliated NiPS<sub>3</sub>.

### **1.3 Outline of thesis**

This thesis investigates the magnetic properties of  $\text{TMPS}_3$  (TM = Fe and Ni) using XMLD-PEEM. Chapters 2 and 3 provide the theoretical and experimental background to elucidate this work, while Chapters 4 and 5 detail the experimental results.

Chapter 2 offers a comprehensive theoretical overview, outlining the X-ray absorption process and deriving X-ray magnetic linear dichroism from the dipole selection rule. Multiplet calculations using the multiplet ligand field model were performed to analyze the X-ray absorption and linear dichroic spectra. The Hamiltonians used in these calculations are explained in the chapter. Magnetic anisotropy and antiferromagnetic domains are briefly introduced as they are investigated using X-PEEM experiments on  $\text{FePS}_3$  and  $\text{NiPS}_3$ . Finally, chapter 3 describes the experimental techniques, including the beamline facility and sample preparation.

Chapter 4 based on [Ref. 1.34] demonstrates the significant magnetic anisotropy in few-layer  $\text{FePS}_3$ . XMLD-PEEM probed the long-range antiferromagnetic order in a temperature- and thickness-dependent manner. Magnetic anisotropy as a function of thickness was estimated from the XMLD spectra. Although magnetic anisotropy decreased in monolayers compared with the bulk samples, spontaneous antiferromagnetic order was preserved down to the monolayer level.

Chapter 5 presents the antiferromagnetic domains in  $\text{NiPS}_3$ , examining these domains in exfoliated  $\text{NiPS}_3$  as a function of temperature. The temperature dependence indicated that domain contrast arises from the antiferromagnetic order, not from crystalline twin defects. Theoretical analysis, Monte Carlo simulations, and multiplet calculations

revealed that small magnetic anisotropy was the primary mechanism underlying NiPS<sub>3</sub> antiferromagnetic domains. Lastly, Chapter 6 provides a summary and outlook for applying XMLD-PEEM in the study of two-dimensional vdW AFMs.

## References

- [Ref. 1.1] Lines, M. *Physics Letters A* **24**, 591-592, (1967).
- [Ref. 1.2] Elmers, H.-J. *International Journal of Modern Physics B* **9**, 3115-3180, (1995).
- [Ref. 1.3] Krasheninnikov, A., Lehtinen, P., Foster, A. S., Pyykkö, P., and Nieminen, R. M. *Physical review letters* **102**, 126807, (2009).
- [Ref. 1.4] Decker, R., Brede, J., Atodiresei, N., Caciuc, V., Blügel, S., and Wiesendanger, R. *Physical Review B* **87**, 041403, (2013).
- [Ref. 1.5] Lee, J.-U., Lee, S., Ryoo, J. H., Kang, S., Kim, T. Y., Kim, P., Park, C.-H., Park, J.-G., and Cheong, H. *Nano Letters* **16**, 7433-7438, (2016).
- [Ref. 1.6] Onsager, L. *Phys. Rev.* **65**, 117-149, (1944).
- [Ref. 1.7] Mermin, N. D. and Wagner, H. *Phys. Rev. Lett.* **17**, 1133, (1966).
- [Ref. 1.8] Kosterlitz, J. M. and Thouless, D. J. *Journal of Physics C: Solid State Physics* **6**, 1181, (1973).
- [Ref. 1.9] Lee, J. U., Lee, S., Ryoo, J. H., Kang, S., Kim, T. Y., Kim, P., Park, C. H., Park, J. G., and Cheong, H. *Nano Lett.* **16**, 7433-7438, (2016).
- [Ref. 1.10] Wildes, A., Rønnow, H. M., Roessli, B., Harris, M., and Godfrey, K. *Phys. Rev. B* **74**, 094422, (2006).

- [Ref. 1.11] Wildes, A. R., Rule, K. C., Bewley, R. I., Enderle, M., and Hicks, T. J. *J. Phys. Condens. Matter* **24**, 416004, (2012).
- [Ref. 1.12] Lançon, D., Walker, H. C., Ressouche, E., Ouladdiaf, B., Rule, K. C., McIntyre, G. J., Hicks, T. J., Rønnow, H. M., and Wildes, A. R. *Phys. Rev. B* **94**, 214407, (2016).
- [Ref. 1.13] Wildes, A. R., Simonet, V., Ressouche, E., McIntyre, G. J., Avdeev, M., Suard, E., Kimber, S. A. J., Lançon, D., Pepe, G., Moubaraki, B., and Hicks, T. J. *Phys. Rev. B* **92**, 224408, (2015).
- [Ref. 1.14] Lançon, D., Ewings, R., Guidi, T., Formisano, F., and Wildes, A. *Physical Review B* **98**, 134414, (2018).
- [Ref. 1.15] Wildes, A., Stewart, J., Le, M., Ewings, R., Rule, K., Deng, G., and Anand, K. *Phys. Rev. B* **106**, 174422, (2022).
- [Ref. 1.16] Scheie, A., Park, P., Villanova, J., Granroth, G., Sarkis, C., Zhang, H., Stone, M., Park, J.-G., Okamoto, S., and Berlijn, T. *arXiv preprint arXiv:2302.07242*, (2023).
- [Ref. 1.17] Joy, P. A. and Vasudevan, S. *Phys. Rev. B* **46**, 5425-5433, (1992).
- [Ref. 1.18] Lim, S. Y., Kim, K., Lee, S., Park, J.-G., and Cheong, H. *Curr. Appl. Phys.* **21**, 1-5, (2021).
- [Ref. 1.19] Ni, Z., Zhang, H., Hopper, D. A., Haglund, A. V., Huang, N., Jariwala, D., Bassett, L. C., Mandrus, D. G., Mele, E. J., and Kane, C. L. *Physical review letters* **127**, 187201, (2021).
- [Ref. 1.20] Kim, K., Lim, S. Y., Lee, J. U., Lee, S., Kim, T. Y., Park, K., Jeon, G. S., Park, C. H., Park, J. G., and Cheong, H. *Nat. Commun.* **10**, 345, (2019).
- [Ref. 1.21] Mc Creary, A., Simpson, J. R., Mai, T. T., McMichael, R. D., Douglas, J. E., Butch, N.,

- Dennis, C., Valdés Aguilar, R., and Hight Walker, A. R. *Phys. Rev. B* **101**, 064416, (2020).
- [Ref. 1.22] Chu, H., Roh, C. J., Island, J. O., Li, C., Lee, S., Chen, J., Park, J.-G., Young, A. F., Lee, J. S., and Hsieh, D. *Phys. Rev. Lett.* **124**, 027601, (2020).
- [Ref. 1.23] Ni, Z., Haglund, A. V., Wang, H., Xu, B., Bernhard, C., Mandrus, D. G., Qian, X., Mele, E. J., Kane, C. L., and Wu, L. *Nature Nanotechnology* **16**, 782-787, (2021).
- [Ref. 1.24] Song, T., Cai, X., Tu, M. W.-Y., Zhang, X., Huang, B., Wilson, N. P., Seyler, K. L., Zhu, L., Taniguchi, T., Watanabe, K., McGuire, M. A., Cobden, D. H., Xiao, D., Yao, W., and Xu, X. *Science* **360**, 1214-1218, (2018).
- [Ref. 1.25] Klein, D. R., MacNeill, D., Lado, J. L., Soriano, D., Navarro-Moratalla, E., Watanabe, K., Taniguchi, T., Manni, S., Canfield, P., Fernández-Rossier, J., and Jarillo-Herrero, P. *Science* **360**, 1218-1222, (2018).
- [Ref. 1.26] Long, G., Henck, H., Gibertini, M., Dumcenco, D., Wang, Z., Taniguchi, T., Watanabe, K., Giannini, E., and Morpurgo, A. F. *Nano Letters* **20**, 2452-2459, (2020).
- [Ref. 1.27] Wu, R., Ross, A., Ding, S., Peng, Y., He, F., Ren, Y., Lebrun, R., Wu, Y., Wang, Z., and Yang, J. *Physical Review Applied* **17**, 064038, (2022).
- [Ref. 1.28] Chen, G., Qi, S., Liu, J., Chen, D., Wang, J., Yan, S., Zhang, Y., Cao, S., Lu, M., Tian, S., Chen, K., Yu, P., Liu, Z., Xie, X. C., Xiao, J., Shindou, R., and Chen, J.-H. *Nature Communications* **12**, 6279, (2021).
- [Ref. 1.29] de Groot, F. M. F. *X-ray absorption of transition metal oxides*. ([SI: sn], 1991).
- [Ref. 1.30] Goedkoop, J. B. *X-ray dichroism of rare earth materials*. ([SI: sn], 1989).
- [Ref. 1.31] Thole, B. T., Van der Laan, G., and Sawatzky, G. A. *Physical review letters* **55**, 2086, (1985).

[Ref. 1.32] van der Laan, G. and Thole, B. T. *Phys Rev B Condens Matter* **43**, 13401-13411,  
(1991).

[Ref. 1.33] Scholl, A., Stöhr, J., Lüning, J., Seo, J. W., Fompeyrine, J., Siegwart, H., Locquet, J.-P.,  
Nolting, F., Anders, S., and Fullerton, E. *Science* **287**, 1014-1016, (2000).

[Ref. 1.34] Lee, Y., Son, S., Kim, C., Kang, S., Shen, J., Kenzelmann, M., Delley, B., Savchenko,  
T., Parchenko, S., and Na, W. *Advanced Electronic Materials*, 2200650, (2022).

## Chapter 2 Theoretical background

### 2.1 X-ray absorption and linear dichroism

#### 2.1.1 X-ray absorption

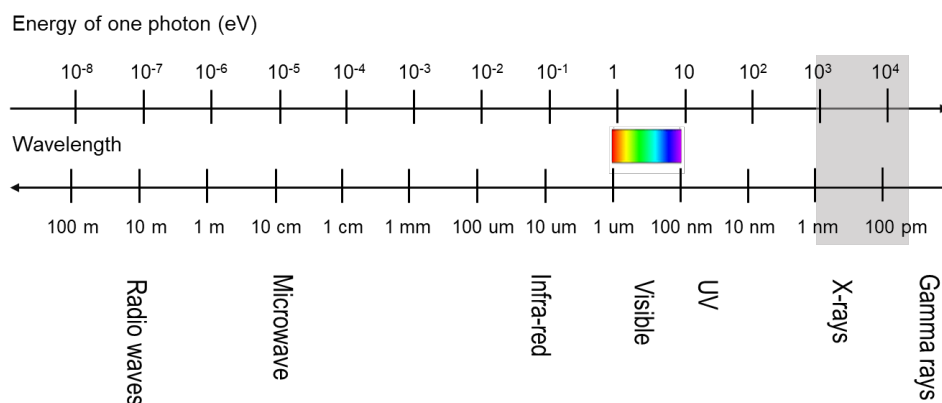


**Figure 2. 1 Energy and wavelength of electromagnetic spectrum**

The resonant light-matter interactions depend on the photon energy of electromagnetic waves. For instance, the infrared energy corresponds to molecular vibrations, and UV and visible light's energy is resonant to valence electrons' hopping. The energy scale of X-ray, which is of interest in this thesis, is in the range of 0.1 to 100 keV, resonant to the core-level electrons.

When X-rays are incident upon the matter, they excite core electrons to empty

valence states, creating core holes. The core holes are re-occupied by electrons from energetically higher states. The additional energy from the re-occupied electrons promotes the emission of fluorescent photons and Auger electrons. The emitted Auger electrons subsequently produce a cascade of secondary electrons. The absorption intensity is measured by detecting the emitted photons or electrons. The escape depths of the emitted Auger and secondary electrons are approximately 0.5 nm and 6 nm, respectively, whereas that of the fluorescent photons is approximately 100 nm.

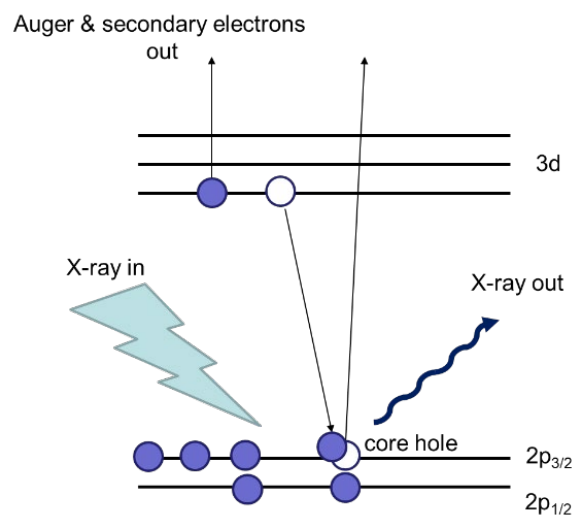


**Figure 2. 2 X-ray absorption process for 3d transition metal atom**

The absorption process follows the selection rule, which conserves the orbital and magnetic moments. This selection rule results in the X-ray magnetic dichroism, as described in the following section.

### 2.1.2 Magnetic linear dichroism in X-ray absorption

Strong X-ray magnetic dichroism (XMD) has been theoretically predicted at the  $M_{4,5}$ -edge of rare-earth materials [Ref. 2.1]. Following the experimental demonstration of XMD in rare-earth compounds using linearly and circularly polarised X-rays [Ref. 2.2], theoretical and experimental investigations on the effect of XMD at the  $L_{2,3}$ -edge of  $3d$  transition metals have been conducted [Ref. 2.3,2.4].

Owing to the spherical symmetry of a free  $3d$  metal atom, the  $3d$  spin-orbit interaction splits the initial state,  $LS$ , into  $LSJ$  levels. These  $(2J+1)$ -fold degenerate states have distinct eigenvalues  $M = -J, -J+1, \dots, J$ , where  $M$  is the component of  $J$  along the quantisation axis. The interatomic exchange interaction can be approximated as an average magnetic field acting on the spin. This exchange field splits the  $(2J+1)$ -fold degenerate states into  $M$  sublevels with energy  $-g\mu_B HM$ . These magnetic sublevels of different  $M$  values induce additional peaks in the  $L_{2,3}$ -edge X-ray absorption spectrum, generating an XMD effect. Note that in the presence of crystal field interactions, the total angular momentum,  $J$ , is an inappropriate quantum number for describing the eigenstates of  $3d$  metal atoms. However, in this study, we ignored the crystal field effect for simplicity.

In the X-ray absorption process below 10 keV photon energy, the electric quadrupole transition is smaller than  $10^{-4}$ ; therefore, the X-ray absorption can be described in terms of the electric dipole transition [Ref. 2.5]. The electric dipole transition from an initial state  $|\alpha JM\rangle$  to a final state  $|\alpha' J' M'\rangle$  is expressed as

$$\sigma_{\alpha JM, \alpha' J' M'} = 4\pi^2 \alpha_0 \hbar \omega \sum_q \left| \langle \alpha JM | P_q^{(1)} | \alpha' J' M' \rangle \right|^2 \delta(E_{\alpha J} - E_{\alpha' J'} + \hbar \omega) \quad (\text{Eq. 2. 1})$$

where  $\alpha$  is the quantum number of the initial state. The photon polarisation is denoted by

$q$ , where  $q = 0$  refers to the electric field vector linearly polarised along the quantisation axis (i.e., the  $z$ -axis), and  $q = \pm 1$  represents left- and right-circularly polarised in the  $xy$ -plane. Based on the Wigner–Eckart theorem, Equation 2.1 can be decomposed into radial and angular parts as follows:

$$\sigma_{\alpha JM, \alpha' J' M'} = 4\pi^2 a_0^2 \hbar \omega S_{\alpha J \alpha' J'} \sum_q \begin{pmatrix} J & 1 & J' \\ -M & q & M' \end{pmatrix}^2 \quad (\text{Eq. 2. 2})$$

where  $S_{\alpha J \alpha' J'} = |\langle \alpha J \| P^{(1)} \| \alpha' J' \rangle|^2$  denotes the line strength of the transition. The optical dipole selection rule restricts the transition under the condition of  $\Delta J = 0, \pm 1$  and  $\Delta M = -q$ . The thermally averaged value is measured experimentally; therefore, the Boltzmann distribution can be applied to Equation 2.2 as follows:

$$\sigma_{\alpha J, \alpha' J'} = 4\pi^2 a_0^2 \hbar \omega S_{\alpha J \alpha' J'} \sum_q A_{JJ'}^q \quad (\text{Eq. 2. 3})$$

$$A_{JJ'}^q = Z^{-1} \sum_M \begin{pmatrix} J & 1 & J' \\ -M & q & M' \end{pmatrix}^2 e^{-M/\theta} \quad \text{with} \quad Z = \sum_M e^{-M/\theta} \quad (\text{Eq. 2. 4})$$

where  $\theta = k_B T / (g\mu_B H)$  is the reduced temperature.

	$q = 0$	$q = \pm 1$
$A_{JJ+1}^q$	$\frac{(J+1)^2 - \langle M^2 \rangle}{(2J+3)(J+1)(2J+1)}$	$\frac{(J+1)(J+2) \pm (2J+3)\langle M \rangle + \langle M^2 \rangle}{2(2J+3)(J+1)(2J+1)}$
$A_{JJ}^q$	$\frac{\langle M^2 \rangle}{J(J+1)(2J+1)}$	$\frac{J(J+1) \mp \langle M \rangle - \langle M^2 \rangle}{2J(J+1)(2J+1)}$
$A_{JJ-1}^q$	$\frac{J^2 - \langle M^2 \rangle}{J(2J-1)(2J+1)}$	$\frac{J(J-1) \mp (2J-1)\langle M \rangle + \langle M^2 \rangle}{2J(2J-1)(2J+1)}$

**Table 2. 1 Expressions  $A_{JJ'}^q$ , from [Ref. 2.6]**

X-ray magnetic linear dichroism (XMLD) intensity can be described using the above expressions for electric field polarisation with  $q$ . The X-ray absorption under a linearly polarised electric field parallel to the magnetisation axis,  $E^{\parallel}$ , is described by a factor  $A_{JJ'}^0$ . In the case of a perpendicular electric field,  $E^{\perp}$ , the X-ray absorption is represented by  $\frac{1}{2}(A_{JJ'}^1 + A_{JJ'}^{-1})$ . The linear dichroism can be defined as the difference between the absorptions under  $E^{\parallel}$  and  $E^{\perp}$ , i.e.,  $E^{\parallel} - E^{\perp} = A_{JJ'}^0 - \frac{1}{2}(A_{JJ'}^1 + A_{JJ'}^{-1})$ , which can be described with  $J$  and magnetizations:

$$\frac{J(J+1) - 3\langle M^2 \rangle}{2(2J+3)(J+1)(2J+1)} \quad \text{for } J' = J+1$$

$$\frac{3\langle M^2 \rangle - J(J+1)}{2J(J+1)(2J+1)} \quad \text{for } J' = J$$

$$\frac{J(J+1) - 3\langle M^2 \rangle}{2J(2J-1)(2J+1)} \quad \text{for } J' = J-1 \quad (\text{Eq. 2.5})$$

The factor  $A_{JJ'}^q$ , for an arbitrary electric field polarisation  $q$  can be expressed in terms of  $A_{JJ'}^0$ ,  $A_{JJ'}^1$ , and  $A_{JJ'}^{-1}$  as follows:

$$A_{JJ'}^0 \cos^2 q + \frac{1}{2}(A_{JJ'}^1 + A_{JJ'}^{-1}) \sin^2 q \quad (\text{Eq. 2.6})$$

The orthogonality relation of the Wigner 3-j symbols yields

$$A_{JJ'}^0 + A_{JJ'}^{-1} + A_{JJ'}^1 = \frac{1}{2J+1} \quad (\text{Eq. 2.7})$$

Therefore,  $A_{JJ'}^q$ , can be written in terms of  $A_{JJ'}^0$ , as follows:

$$A_{JJ'}^q = \frac{1 + (3(2J+1)A_{JJ'}^0 - 1)C_q}{3(2J+1)} \quad (\text{Eq. 2.8})$$

$$\text{where } C_q = \frac{3}{2}\cos^2q - \frac{1}{2} \quad (\text{Eq. 2.9})$$

The XMLD intensity can be expressed as a function of  $\langle M^2 \rangle$  and  $\cos^2q$  using Equation 2.8-9 and the expression of  $A_{JJ'}^0$ , which contains  $\langle M^2 \rangle$  terms [Ref. 2.7,2.8].

$$I(\theta, T) = a + b(3\cos^2q - 1)\langle M^2 \rangle_T \quad (\text{Eq. 2.10})$$

The XMLD intensity is proportional to the square of the local magnetisation. The magnetic order of antiferromagnets can be probed even though they have zero net magnetisation.

### 2.1.3 Multiplet calculation

In the study presented in this thesis, we restricted the materials to  $3d$  transition metal compounds, particularly  $TMPS_3$ , for which the X-ray absorption process is an excitation from  $2p^6d^n$  to  $2p^5d^{n+1}$ . For each  $TMPS_3$  ( $TM = \text{Mn, Ni, and Fe}$ ), we considered a single  $TMS_6$  cluster for the X-ray absorption spectra. Calculating multiplets and their excitations on a single  $TMS_6$  cluster was sufficient for the X-ray absorption spectra because we considered the localised orbitals in the insulator and the localised absorption process in the X-ray regime. Finally, we employed the multiplet ligand field theory, considering  $3d$  correlation and  $3d$ -ligand orbital hybridisation.

We used Quany, a quantum many-body code, to reproduce the experimental X-ray absorption and linear dichroism spectra [Ref. 2.9]. The script language defined operators in the second quantisation and calculated the eigenstates of Green's functions for

these operators [Ref. 2.10].

$$H = H_{ee} + H_{SO} + H_{CF} + H_{LF} + H_{ex} \text{ (Eq. 2. 11)}$$

### **Electron–electron interaction ( $H_{ee}$ )**

From the second quantisation and spherical harmonic representations, the Hamiltonian of the Coulomb repulsion interaction in  $3d$  orbitals can be written as [Ref. 2.11]

$$\sum_{i,j} \frac{1}{2} \frac{e^2}{|r_i - r_j|} = \sum_{\tau_1, \tau_2, \tau_3, \tau_4} U_{\tau_1, \tau_2, \tau_3, \tau_4} d_{\tau_1}^\dagger d_{\tau_2}^\dagger d_{\tau_3} d_{\tau_4} \text{ (Eq. 2. 12)}$$

with

$$U_{\tau_1, \tau_2, \tau_3, \tau_4} = -\frac{1}{2} \delta_{\sigma_1, \sigma_2} \delta_{\sigma_3, \sigma_4} \sum_{k=0,2,4} C^{(k)}[l_1=2, m_1; l_3=2, m_3] C^{(k)}[l_4=2, m_4; l_2=2, m_2] F_{dd}^k \text{ (Eq. 2. 13)}$$

$$\text{and } C^{(k)}[l_1, m_1; l_2, m_2] = \langle Y_{m_1}^{l_1} | C_{m_1 - m_2}^{(k)} | Y_{m_2}^{l_2} \rangle \text{ where } C_m^{(k)} = \sqrt{\frac{4\pi}{2k+1}} Y_m^k \text{ (Eq. 2. 14)}$$

Above,  $\tau$  denotes the combined spin and orbital,  $\sigma$  is the spin, and  $l$  and  $m$  are the angular momentum indices.  $F^k$  denotes the radial Slater integrals, which can be calculated using the Hartree–Fock approximation of a free ion using Cowan’s code [Ref. 2.12]. Slater integral  $F^0$  is related to Hubbard energy, and  $F^2$  and  $F^4$  are related to Hund’s energy [Ref. 2.13]. The Slater integral values of a free atom from the Hartree–Fock approximation are reduced in a crystal owing to the screening effect. Similar to  $3d$  electrons, the Hamiltonian of the Coulomb repulsion and exchange interactions between the  $2p$  and  $3d$  orbital electrons of the transition metal can be expressed as

$$\sum_{\tau_1, \tau_2, \tau_3, \tau_4} 2U_{\tau_1, \tau_2, \tau_3, \tau_4}^G d_{\tau_1}^\dagger p_{\tau_2}^\dagger d_{\tau_3} p_{\tau_4} + 2U_{\tau_1, \tau_2, \tau_3, \tau_4}^F d_{\tau_1}^\dagger p_{\tau_2}^\dagger d_{\tau_3} p_{\tau_4} \text{ (Eq. 2. 15)}$$

with

$$U_{\tau_1, \tau_2, \tau_3, \tau_4}^F = -\frac{1}{2} \delta_{\sigma_1, \sigma_2} \delta_{\sigma_3, \sigma_4} \sum_{k=0,2} C^{(k)} \left[ l_1=2, m_1; l_3=2, m_3 \right] C^{(k)} \left[ l_4=2, m_4; l_2=2, m_2 \right] F_{pd}^k \quad (\text{Eq. 2.16})$$

and

$$U_{\tau_1, \tau_2, \tau_3, \tau_4}^G = -\frac{1}{2} \delta_{\sigma_1, \sigma_2} \delta_{\sigma_3, \sigma_4} \sum_{k=1,3} C^{(k)} \left[ l_1=2, m_1; l_3=1, m_3 \right] C^{(k)} \left[ l_4=2, m_4; l_2=1, m_2 \right] G_{pd}^k \quad (\text{Eq. 2.17})$$

Above,  $G^k$  represents the radial Slater integrals for exchange interactions, which can also be calculated using the Hartree–Fock approximation.

### **Spin–orbit coupling ( $H_{SO}$ )**

In this study, the spin–orbit coupling of the  $2p$  core hole and  $d$  orbitals were included.

$$H_{SO} = \sum_i \xi(r_i) l_i \cdot s_i \quad (\text{Eq. 2.18})$$

The  $2p$  core hole spin–orbit coupling splits an  $L$ -edge absorption spectrum into two peaks: a lower  $L_3$  peak associated with transitions from  $2p_{3/2}$  and a higher  $L_2$  peak related to  $2p_{1/2}$  to  $d$  orbital transitions.

### **Crystal field ( $H_{CF}$ )**

The orbital symmetry of a free atom is spherical. However, when an atom is in a crystal, the spherical symmetry is broken by the electric field of the neighbouring atoms. This resultant electric field is called the crystal (electric) field, and the detailed form of it

depends on the local symmetry. The Hamiltonian of the crystal field can be described based on spherical harmonics as follows:

$$H_{CF} = \sum_{k=0}^{\infty} \sum_{m=-k}^k A_{k,m} C_k^m(\theta, \phi)$$

$$\text{with } C_k^m(\theta, \phi) = \left(\frac{4\pi}{2k+1}\right)^2 Y_{k,m}(\theta, \phi) \text{ (Eq. 2. 19)}$$

The expansion coefficient,  $A_{k,m}$ , is a crystal field parameter determined by the local symmetry.

The low symmetry of a crystal field can result in natural and/or magnetic anisotropy. In the case of  $TMPS_3$ , each transition metal ion is surrounded by six sulfur ions. The  $TMS_6$  octahedra have a slight trigonal distortion, causing the point-group symmetry of the metal ions to be lowered from  $O_h$  to  $D_{3d}$  [Ref. 2.14,2.15]. For  $FePS_3$ , the trigonal elongation of  $FeS_6$  splits the  $t_{2g}$  orbitals into a lower doublet  $e_{g\pi}$  orbital and a higher singlet  $a_{1g}$  orbital. This further orbital splitting results in a large magnetic anisotropy combined with the spin-orbit interaction, which is discussed in more detail in Chapter 4.

### **Ligand field ( $H_{LF}$ )**

The ligand field theory considers a transition metal solid as the  $d$  shell of a single transition metal atom surrounded by a ligand shell. Therefore, the onsite splitting of the transition metal orbitals and the ligand shell must be considered. The covalency should be accounted for by adding a hopping term to the calculation.

A  $\text{TMS}_6$  cluster has 10  $3d$  orbitals from the single transition metal atom and 36  $2p$  orbitals from the 6 sulfur atoms. Reference 2.7 demonstrated that 6  $S$ - $2p$  shells could be described as an effective ligand  $d$  shell having the same symmetry as the  $3d$  orbitals of the transition metal. This reduces the number of orbitals required for computation from 46 (10  $3d$  orbitals and 36  $2p$  orbitals) to 20 (10  $3d$  orbitals and 10 effective ligand  $d$  orbitals), significantly decreasing the computing time.

The onsite energies of the  $3d$  and  $2p$  orbitals of the transition metal atom are defined as

$$\varepsilon_d \sum_{\tau} d_{\tau}^{\dagger} d_{\tau} + \varepsilon_p \sum_{\tau} p_{\tau}^{\dagger} p_{\tau} \quad (\text{Eq. 2. 20})$$

$$\text{with } \varepsilon_d = \left[ 10\Delta - n_d(31 + n_d)U_{dd}/2 - 90U_{pd} \right] / (16 + n_d) \quad (\text{Eq. 2. 21})$$

$$\text{and } \varepsilon_p = \left[ 10\Delta + (1 + n_d) \left\{ n_d U_{dd}/2 - (10 + n_d)U_{pd} \right\} \right] / (16 + n_d) \quad (\text{Eq. 2. 22})$$

Above,  $\tau$  denotes the  $3d$  and  $2p$  orbitals and  $\Delta$  is the charge transfer energy.

The onsite energy of the ligand shell is defined using the same method as that used for the  $3d$  orbitals.

$$\varepsilon_L \sum_{\tau} L_{\tau}^{\dagger} L_{\tau} + H_{CEF}^L \quad (\text{Eq. 2. 23})$$

$$\text{with } \varepsilon_L = \left[ (1 + n_d) \left( n_d U_{dd}/2 + 6U_{pd} \right) - (6 + n_d)\Delta \right] / (16 + n_d) \quad (\text{Eq. 2. 24})$$

The  $H_{CEF}^L$  term is the crystal field Hamiltonian of the ligand shell defined by the same crystal field symmetry as considered for the  $3d$  orbitals of the transition metal.

The hopping term is treated as the effective potential.  $V(\Gamma)$  is the hopping strength between the  $3d$  and ligand orbitals, where  $\Gamma$  and  $\tau$  represent the orbital symmetry, such as

$t_{2g}$ , and an individual orbital, respectively.

$$H = \sum_T \left[ V(T) \sum_{\tau \in T} (d_{\tau}^{\dagger} L_{\tau} + L_{\tau}^{\dagger} d_{\tau}) \right] \text{ (Eq. 2. 25)}$$

### **Exchange field ( $H_{ex}$ )**

An exchange field term was introduced to account for the long-range magnetic order in the material.

$$H_{ex} = \sum_i J \langle S_i \rangle \text{ (Eq. 2. 26)}$$

This field acts only on spins, whereas the magnetic field operates on both spins and orbitals. For example, the magnetic order of antiferromagnetic NiO is reproduced by an exchange field of  $6 \times 27 \text{ meV}$ , considering the superexchange interactions between an oxygen atom and its six nearest neighbouring Ni ions [Ref. 2.7,2.16].

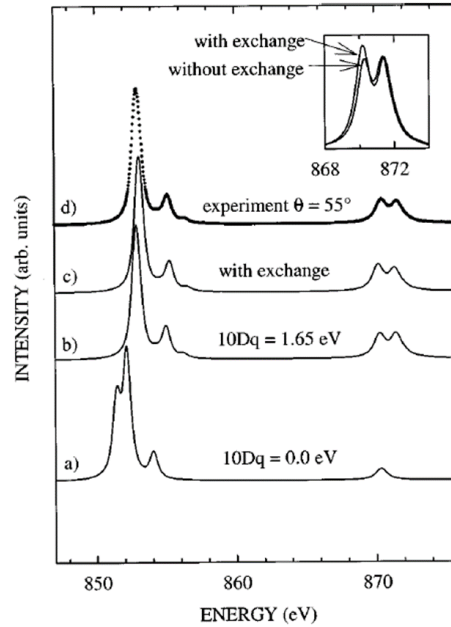


**Figure 2. 3 Ni L<sub>2,3</sub>-edge X-ray absorption spectra of NiO with/without crystal and exchange fields [Ref. 2.7].**

## 2.2 Magnetic anisotropy

Magnetic anisotropy refers to the energy dependence of magnetisation direction. The easy axis represents the direction with the lowest energy of magnetisation, which is the preferred magnetisation direction. The exchange interaction in spins does not break the rotational symmetry of the spin quantisation axis, i.e., the spin quantisation axis is isotropic. To explain magnetic anisotropy, the concepts of dipole–dipole interactions and spin–orbit coupling are applied.

Magnetocrystalline anisotropy energy is the change in the free energy of a crystal with the rotation of magnetisation. Van Vleck first proposed magnetocrystalline anisotropy

as a consequence of the spin–orbit interaction that couples an isotropic spin moment to an anisotropic lattice [Ref. 2.17]. Bruno further developed a perturbation theory with spin–orbit interaction to explain the magnetocrystalline anisotropy of a  $3d$  transition metal monolayer [Ref. 2.18,2.19]. The spin–orbit coupling constant of  $3d$  transition metals is about 50–100 meV, which is small compared to the bandwidth of a few electronvolts. Therefore, the spin–orbit interaction can be treated as a perturbation term for energy correction. Theoretically, magnetocrystalline anisotropy is proportional to the anisotropy of the orbital momentum.

### **2.3 Antiferromagnetic domain**

In the case of ferromagnets, magnetic domain formation is relatively straightforward. A ferromagnetic domain originates from the minimisation of the free energy in the presence of a stray field from its magnetisation. Antiferromagnetic domains, however, are not as intuitive as ferromagnetic domains because there is no macroscopic stray field [Ref. 2.20]. Typically, the domains in antiferromagnets are explained in terms of structural defects such as crystalline twins or Néel vector rotations in materials with weak magnetic anisotropy.

Domains in epitaxial antiferromagnetic films have been investigated to study the exchange bias effect in ferromagnet/antiferromagnet heterostructures [Ref. 2.21] and Néel spin–orbit torque devices [Ref. 2.22,2.23,2.24]. The substrate-clamping effect is emphasised in thin films of NiO and  $\alpha$ -Fe<sub>2</sub>O<sub>3</sub> [Ref. 2.25,2.26]. In these cases, the incompatibility between the spontaneous magnetoelastic strain in an antiferromagnetic film and the non-deformation in a nonmagnetic substrate induces a destressing field. The

multidomain state lowers the free energy from the destressing field, reducing the average strain to zero, with the opposite sign of the shear stress in different domains. Tetragonal CuMnAs has been considered a promising material for antiferromagnetic spintronics, as it demonstrates current-induced antiferromagnetic domain switching and operation of all-electrical memory bits [Ref. 2.22]. Scanning transmission electron microscopy and XMLD-photoelectron emission microscopy images have also revealed that the microscopic antiferromagnetic domain structure in CuMnAs is influenced mainly by nanoscale twin defects [Ref. 2.27,2.28]. Similarly, the antiferromagnetic epitaxial film of LaFeO<sub>3</sub> has a multidomain state coupled with structural twin domains [Ref. 2.29,2.30].

## References

- [Ref. 2.1] Thole, B. T., Van der Laan, G., and Sawatzky, G. A. *Physical review letters* **55**, 2086, (1985).
- [Ref. 2.2] van der Laan, G., Thole, B. T., Sawatzky, G. A., Goedkoop, J. B., Fuggle, J. C., Esteva, J.-M., Karnatak, R., Remeika, J., and Dabkowska, H. A. *Physical Review B* **34**, 6529, (1986).
- [Ref. 2.3] van der Laan, G. and Thole, B. T. *Phys Rev B Condens Matter* **43**, 13401-13411, (1991).
- [Ref. 2.4] Kuiper, P., Searle, B. G., Rudolf, P., Tjeng, L. H., and Chen, C. T. *Phys Rev Lett* **70**, 1549-1552, (1993).
- [Ref. 2.5] De Groot, F. and Kotani, A. *Core level spectroscopy of solids*. (CRC press, 2008).
- [Ref. 2.6] Goedkoop, J. B. *X-ray dichroism of rare earth materials*. ([SI: sn], 1989).
- [Ref. 2.7] Alders, D., Tjeng, L. H., Voogt, F. C., Hibma, T., Sawatzky, G. A., Chen, C. T., Vogel, J.,

- Sacchi, M., and Iacobucci, S. *Physical Review B* **57**, 11623-11631, (1998).
- [Ref. 2.8] Stöhr, J., Scholl, A., Regan, T., Anders, S., Lüning, J., Scheinfein, M., Padmore, H., and White, R. *Physical review letters* **83**, 1862, (1999).
- [Ref. 2.9] Haverkort, M. W., Zwierzycki, M., and Andersen, O. K. *Phys. Rev. B* **85**, 165113, (2012).
- [Ref. 2.10] de Groot, F. M., Elnaggar, H., Frati, F., Wang, R.-p., Delgado-Jaime, M. U., van Veenendaal, M., Fernandez-Rodriguez, J., Haverkort, M. W., Green, R. J., and van der Laan, G. *Journal of Electron Spectroscopy and Related Phenomena* **249**, 147061, (2021).
- [Ref. 2.11] Zhang, Y., Xie, R., Long, T., Günzing, D., Wende, H., Ollefs, K. J., and Zhang, H. *npj Computational Materials* **9**, 46, (2023).
- [Ref. 2.12] Cowan, R. D. *The theory of atomic structure and spectra*. (Univ of California Press, 1981).
- [Ref. 2.13] de Groot, F. in *AIP Conference Proceedings*. 497-520 (American Institute of Physics).
- [Ref. 2.14] Joy, P. A. and Vasudevan, S. *Phys. Rev. B* **46**, 5425-5433, (1992).
- [Ref. 2.15] Joy, P. and Vasudevan, S. *Phys. Rev. B* **46**, 5134, (1992).
- [Ref. 2.16] Alders, D., Vogei, J., Levelut, C., Peacor, S., Hibma, T., Sacchi, M., Tjeng, L., Chen, C., Van der Laan, G., and Thole, B. *EPL (Europhysics Letters)* **32**, 259, (1995).
- [Ref. 2.17] van Vleck, J. H. *Physical Review* **52**, 1178, (1937).
- [Ref. 2.18] Bruno, P. *Phys. Rev. B* **39**, 865, (1989).
- [Ref. 2.19] van der Laan, G. *Journal of Physics: Condensed Matter* **10**, 3239, (1998).
- [Ref. 2.20] Tanner, B. *Contemporary Physics* **20**, 187-210, (1979).
- [Ref. 2.21] Ohldag, H., Scholl, A., Nolting, F., Anders, S., Hillebrecht, F. U., and Stöhr, J. *Physical review letters* **86**, 2878-2881, (2001).

- [Ref. 2.22] Wadley, P., Reimers, S., Grzybowski, M. J., Andrews, C., Wang, M., Chauhan, J. S., Gallagher, B. L., Campion, R. P., Edmonds, K. W., Dhesi, S. S., Maccherozzi, F., Novak, V., Wunderlich, J., and Jungwirth, T. *Nature Nanotechnology* **13**, 362-365, (2018).
- [Ref. 2.23] Baldrati, L., Gomony, O., Ross, A., Filianina, M., Lebrun, R., Ramos, R., Leveille, C., Fuhrmann, F., Forrest, T. R., Maccherozzi, F., Valencia, S., Kronast, F., Saitoh, E., Sinova, J., and Kläui, M. *Physical review letters* **123**, 177201, (2019).
- [Ref. 2.24] Wadley, P., Howells, B., Železný, J., Andrews, C., Hills, V., Campion, R. P., Novák, V., Olejník, K., Maccherozzi, F., Dhesi, S. S., Martin, S. Y., Wagner, T., Wunderlich, J., Freimuth, F., Mokrousov, Y., Kuneš, J., Chauhan, J. S., Grzybowski, M. J., Rushforth, A. W., Edmonds, K. W., Gallagher, B. L., and Jungwirth, T. *Science* **351**, 587-590, (2016).
- [Ref. 2.25] Baldrati, L., Ross, A., Niizeki, T., Schneider, C., Ramos, R., Cramer, J., Gomony, O., Filianina, M., Savchenko, T., Heinze, D., Kleibert, A., Saitoh, E., Sinova, J., and Kläui, M. *Physical Review B* **98**, 024422, (2018).
- [Ref. 2.26] Wittmann, A., Gomony, O., Litzius, K., Kaczmarek, A., Kossak, A. E., Wolf, D., Lubk, A., Johnson, T. N., Trensina, E. A., and Churikova, A. *Physical Review B* **106**, 224419, (2022).
- [Ref. 2.27] Reimers, S., Kriegner, D., Gomony, O., Carbone, D., Krizek, F., Novák, V., Campion, R. P., Maccherozzi, F., Björling, A., Amin, O. J., Barton, L. X., Poole, S. F., Omari, K. A., Michalička, J., Man, O., Sinova, J., Jungwirth, T., Wadley, P., Dhesi, S. S., and Edmonds, K. W. *Nature Communications* **13**, 724, (2022).
- [Ref. 2.28] Krizek, F., Reimers, S., Kašpar, Z., Marmodoro, A., Michalička, J., Man, O., Edström, A., Amin, O. J., Edmonds, K. W., Campion, R. P., Maccherozzi, F., Dhesi, S. S., Zubáč, J.,

Kriegner, D., Carbone, D., Železný, J., Výborný, K., Olejník, K., Novák, V., Ruzs, J.,  
Idrobo, J.-C., Wadley, P., and Jungwirth, T. *Science Advances* **8**, eabn3535, (2022).

[Ref. 2.29] Lüning, J., Nolting, F., Scholl, A., Ohldag, H., Seo, J. W., Fompeyrine, J., Locquet, J. P.,  
and Stöhr, J. *Physical Review B* **67**, (2003).

[Ref. 2.30] Hallsteinsen, I., Moreau, M., Chopdekar, R., Christiansen, E., Nord, M., Vullum, P.-E.,  
Grepstad, J., Holmestad, R., Selbach, S. M., and Scholl, A. *Apl Materials* **5**, 086107, (2017).

## **Chapter 3**

### **Experimental techniques**

#### **3.1 X-ray photoemission microscopy (XPEEM) in SIM beamline**

The XPEEM experiments were performed at the surface/interface: microscopy (SIM) beamline at the Swiss Light Source (SLS), Switzerland.

##### **3.1.1 Synchrotron radiation**

The SLS accelerator facility comprises three major parts: a linear accelerator (Linac), a booster synchrotron, and a storage ring. First, electrons are accelerated in a Linac and booster synchrotron to attain light speed and are fed into a storage ring. The magnets in the storage ring allow electrons to undergo centripetal acceleration, resulting in the emission of electromagnetic radiation. The SIM beamline covers a photon energy range of 90 eV–2 keV [Ref. 3.1]. High-flux light and variable polarisation are generated by insertion devices called undulators. The SIM beamline consists of two Apple II-type undulators, a plane grating monochromator, and other optics, such as plane mirrors, that provide variable polarisation and collimated light [Ref. 3.1].

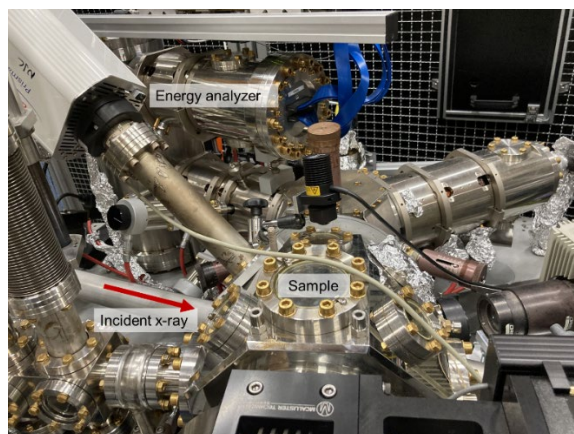
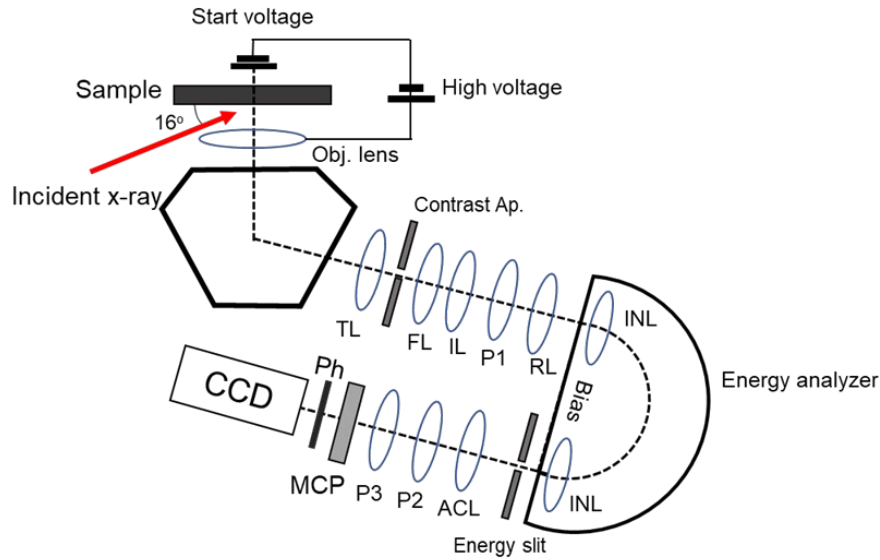


Figure 3. 1 PEEM setup in SIM beamline in SLS.

### 3.1.2. XPEEM equipment and experiment

A commercial PEEM (Elimitec GmbH) is installed on the SIM beamline. A schematic of the experimental setup is shown in Figs. 3.1 and 3.2. Polarised and monochromatic X-rays impinged on the sample at a grazing angle of  $16^\circ$ . A small grazing angle increases the scattering cross-section on the surface, enhancing the surface sensitivity of XPEEM. The horizontal footprint of the X-rays on the sample was fixed with a full width at half maximum (FWHM) of  $\sim 220 \mu\text{m}$ , and the vertical footprint was determined by the exit slit size of the beamline, which is usually  $50\text{--}150 \mu\text{m}$  for the PEEM experiment [Ref. 3.2]. The typical imaging field of view in the experiment was approximately  $20\text{--}50 \mu\text{m}$ , which is smaller than the sample spot size, guaranteeing uniform illumination of the sample. A high voltage of 20 kV was applied between the sample and objective lens to accelerate the emitted photoelectrons towards the magnetic lenses of the microscope [Ref. 3.2].



**Figure 3.2 Schematic image of XPEEM in the SIM beamline.** TL: transfer lens; FL: field lens; IL: illumination lens; P1, 2, 3: Projective lens 1, 2, 3; RL: Rt. Lens; INL: interm. lens; ACL: Accelerating lens

A series of electromagnetic lenses magnify the lateral distribution of the electrons. Deflectors and stigmators were adjusted to optimise the electron path and correct image distortion. All the lenses and stigmators must be aligned repeatedly to obtain focused and undistorted images. The energy analyser enables the energy selection of electrons by changing the “start voltage”, which enhances the spatial resolution. The electrons passing through the electromagnetic optical components were projected onto a multichannel electron plate (MCP) intensifier and converted to visible light by a phosphor screen. The converted light was detected using a two-dimensional CCD camera.

The intensity of the emitted electrons is proportional to the absorption coefficient. Therefore, information about the local X-ray absorption (XA) coefficient can be obtained by investigating the local electron yield intensity [Ref. 3.3,3.4]. The local electron intensity

was recorded in the XPEEM images with a spatial resolution. XA spectra of the region of interest (ROI) can be obtained from a series of XPEEM images at successive photon energies (Fig. 3.3). In addition, the image processing program *Image J* was used for data processing, including drift correction, extraction of the intensity of ROI, and pixel-wise calculation of X-ray intensities.

The sample temperature was controlled by balancing the liquid helium's cooling power and the filament's heating power on the sample holder. Next, a platinum thermometer was connected to the sample holder to monitor its temperature.

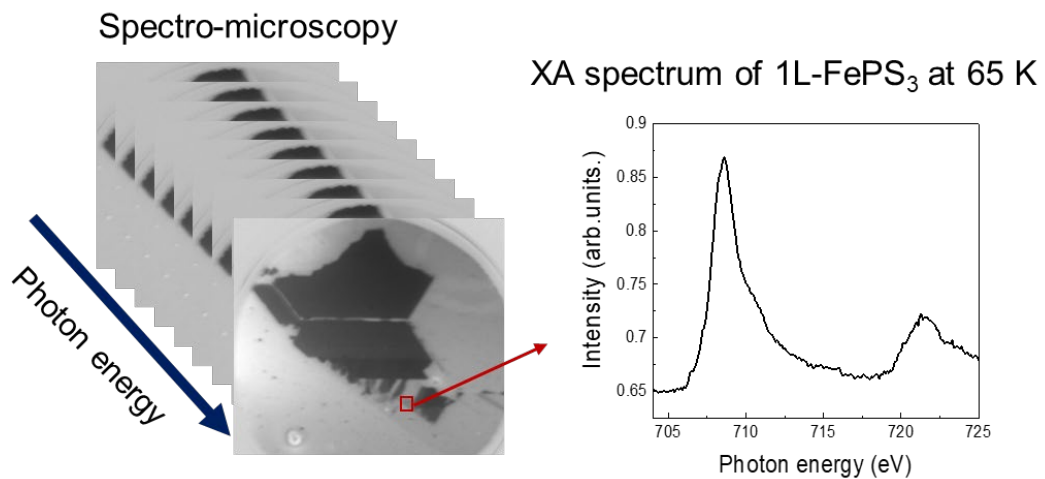


**Figure 3.3 Extraction of XA spectrum of the ROI from the successive XPEEM images.** The sequence of XPEEM images with successive photon energy with ROI notated using the red box (left) and the extracted XA spectrum of ROI with the *Image J* program (right).

## **3.2 Sample preparation**

### **3.2.1 Lithography of the gold marker**

To identify the positions of the exfoliated flakes, Au markers were patterned on the substrates using photolithography, followed by titanium/gold evaporation. Before photolithography, the substrates were cleaned in an ultrasonic bath with acetone and IPA solutions and dried using nitrogen gas. The photoresist (AZ 5214E) was uniformly spread by spin coating at 4000 rpm for 60 s, followed by soft-baking at 90 °C for 60 s. The sample was exposed to UV light with a wavelength of 365 nm and an intensity of approximately 25 mW/cm<sup>2</sup> for 40 s (MDA-400S, MIDAS). The sample was developed in a MIF 300 developer for 50 s and then rinsed with deionised water. We deposited titanium 3 nm/gold 20 nm using an e-beam evaporator. The lift-off process was performed by soaking and sonicating the samples in acetone.

### **3.2.2 Exfoliation of a single crystal**

We exfoliated a single crystal using a mechanical method with sticky tape (Fig. 3.4). Just before exfoliation, the patterned substrates were cleaned with acetone and IPA through sonication to remove organic contamination from the substrate surface. The single crystal was cleaved several times using Scotch tape. They were then transferred onto the prepared substrate. The samples for the experiment were selected based on their colour, rough index of flake thickness, and lateral size using optical microscopy images. The accurate thickness was determined using atomic force microscopy (AFM). Finally, the sample for the experiment was determined using AFM data, such as thickness, flatness, and lateral size. All processes were performed in an argon-filled glove box.

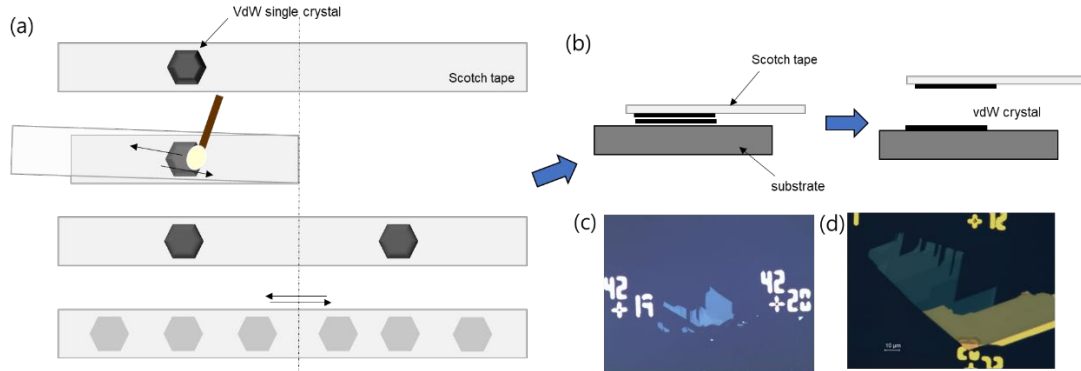


**Figure 3.4 Exfoliation of van der Waals single crystal.** (a) Cleaving bulk van der Waals crystal with Scotch tape. The crystal gets thinner by folding the Scotch tape in half with a gentle cotton swab rub on the tape and unfolding it repeatedly. (b) Transfer of thin crystal onto the substrate. The optical microscopy images of exfoliated (c) FePS<sub>3</sub> and (d) NiPS<sub>3</sub> on the ITO/Si substrate. The scale is the same in (c) and (d).

### 3.2.3 Optimal substrate for charging issues

The studied material, TMPS<sub>3</sub> [TM = Fe, Ni], is insulating; therefore, probing it using photoemitted electrons can cause charging problems on the surface. Dr Suhan Son tried several types of substrates to solve the charging issues and found that an indium-tin oxide (ITO) substrate was the best option for X-PEEM experiments on insulators. The results are summarised in this section.

We prepared an exfoliated NiPS<sub>3</sub> sample on two substrates: ITO (70 nm)/Si and SiO<sub>2</sub> (90 nm)/Si. Two samples were prepared using the method described in Sections 3.3.1 and 3.3.2. After exfoliation, we patterned a 10 nm thick gold window on the target NiPS<sub>3</sub> flake on the SiO<sub>2</sub> substrate to discharge secondary electrons through the gold pattern (Fig. 3.5 (e)). The resolution of the XPEEM image of the ITO sample was better than that of the SiO<sub>2</sub> sample; however, the XPEEM images did not show significant differences between the two samples (Fig. 3.5). The XA spectra from the XPEEM images demonstrated the

superiority of the ITO-coated Si substrate. The XA spectrum of bulk NiPS<sub>3</sub> on the ITO substrate showed clear Ni  $L_2$  and  $L_3$  resonance peaks (Fig. 3.6(a)). The bilayer exhibits broader peaks than the bulk layer; however, two prominent resonance peaks are observed (Fig. 3.6(b)). Significant distortion of the XA spectrum was observed in the bilayer NiPS<sub>3</sub> on the SiO<sub>2</sub> substrate (Fig. 3.6(c)). The charging effect resulted in indistinguishable  $L_2$  and  $L_3$  peaks with low signal-to-noise ratios. After optimising the right substrate, we adopted the ITO/Si substrate for the successive XPEEM experiment with TMPS<sub>3</sub>. The successful measurement of monolayer FePS<sub>3</sub> demonstrates the excellent performance of the ITO/Si substrate for the XPEEM experiment, which is described in Chapter 4.

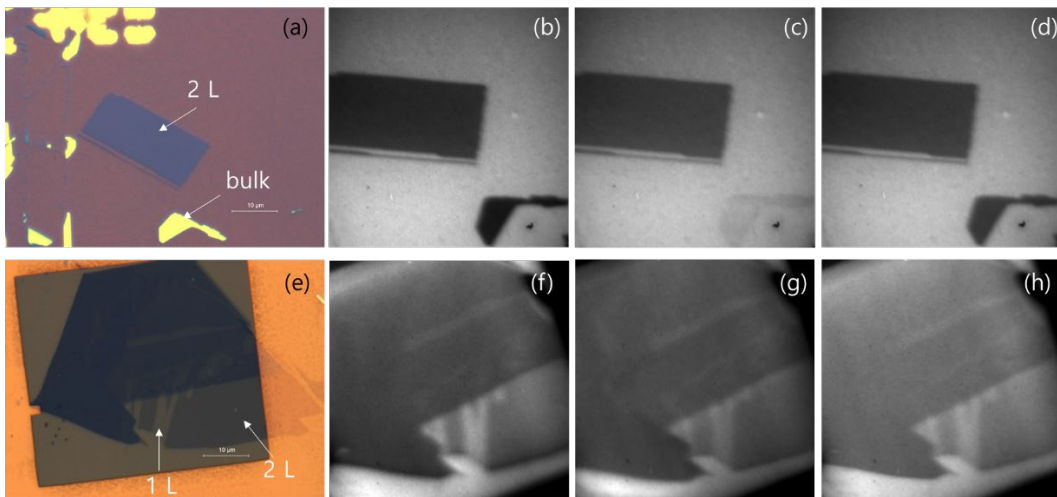


**Figure 3.5** OM and XPEEM images of exfoliated NiPS<sub>3</sub> on (a–d) an ITO/Si substrate and (e–h) a SiO<sub>2</sub> substrate with the gold window. The photon energies of XPEEM images were 846, 853, and 854.1 eV for the second, third, and fourth columns, respectively.

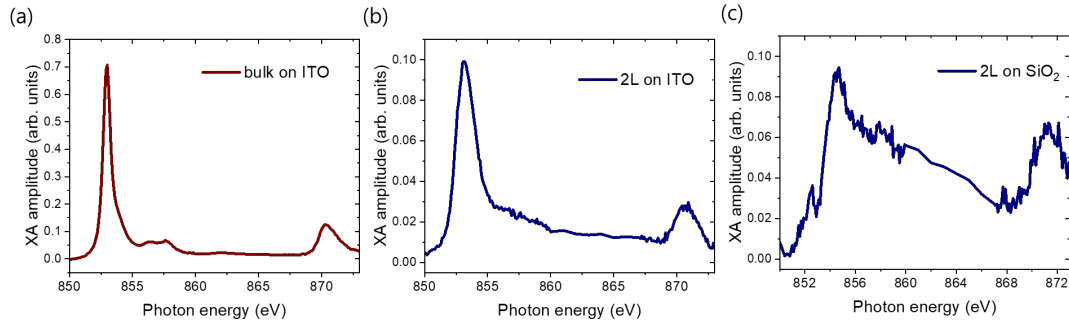


**Figure 3.6** XA spectra of Ni  $L_{2,3}$ -edge from (a) bulk, (b) 2L on the ITO/Si substrate, and (c) 2L NiPS<sub>3</sub> on the SiO<sub>2</sub> substrate with the gold window. XA spectra were extracted from the successive XPEEM images shown in Fig. 3.5.

## References

- [Ref. 3.1] Flechsig, U., Nolting, F., Fraile Rodriguez, A., Krempaský, J., Quitmann, C., Schmidt, T., Spielmann, S. and Zimoch, D. in *AIP Conference Proceedings*. 319-322 (American Institute of Physics).
- [Ref. 3.2] Le Guyader, L., Kleibert, A., Rodríguez, A. F., El Moussaoui, S., Balan, A., Buzzi, M., Raabe, J. and Nolting, F. *Journal of Electron Spectroscopy and Related Phenomena* **185**, 371-380, (2012).
- [Ref. 3.3] Beaurepaire, E., Scheurer, F., Krill, G. and Kappler, J.-P. *Magnetism and synchrotron radiation*. Vol. 34 (Springer, 2001).
- [Ref. 3.4] de Groot, F. M. F. *X-ray absorption of transition metal oxides*. ([SI: sn], 1991).

## **Chapter 4**

# **Large magnetic anisotropy in the few-layer vdW antiferromagnet FePS<sub>3</sub>**

### **4.1 Introduction**

According to the Mermin-Wagner theorem, the long-range magnetic order cannot exist in a two-dimensional magnet at a finite temperature without magnetic anisotropy [Ref. 4.1]. Magnetic anisotropy protects the long-range magnetic order against enhanced thermal spin fluctuations due to the low dimensionality. Therefore, it has become a crucial area of research to understand the origin and means of controlling magnetic anisotropy in two-dimensional van der Waals magnets [Ref. 4.2,4.3,4.4,4.5]

One important point relevant to this work is that the contribution of orbitals to magnetism is often disregarded in *3d* transition metal compounds because the magnetic orbital moment is commonly believed to be suppressed in most *3d* transition metals by the crystal field effect. However, the system with reduced symmetry can host sizeable magnetic orbital moments [Ref. 4.6]. This big magnetic orbital moment can give rise to magnetic anisotropy in combination with the spin-orbit coupling effect.

FePS<sub>3</sub> is a van der Waals antiferromagnet and a representative 2D Ising system. A previous Raman study on few-layer FePS<sub>3</sub> showed the presence of long-range magnetic order in a monolayer successively [Ref. 4.7]. However, they could not quantitatively

analyze the magnetic anisotropies and their origins in the few-layer regime because of technical limitations.

Here, we demonstrate the persistence of long-range magnetic order down to the monolayer and estimate the magnetic anisotropy using XMLD-PEEM. Finally, XMLD-PEEM provides direct access to the spin and orbital moments, allowing for an investigation into the microscopic origins of the strong magnetic anisotropy.

## **4.2 Van der Waals Ising antiferromagnet FePS<sub>3</sub>**

FePS<sub>3</sub> is an Ising-type antiferromagnet, where spins are aligned along the  $c^*$ -axis. The Fe ions are arranged in a honeycomb lattice with ferromagnetic zig-zag spin chains.

Neighboring ferromagnetic zig-zag spin chains are coupled antiferromagnetically to each other (Figure 4.1 (a)). The out-of-plane magnetic susceptibility is larger than the in-plane susceptibility, which indicates a significant magnetic anisotropy in bulk FePS<sub>3</sub>, even in the paramagnetic phase (Figure 4.1(b)). The strong easy-axis magnetic anisotropy allows the magnetic moments to persist down to the monolayer, as predicted theoretically by Onsager's solution [Ref. 4.8]. The first experimental evidence of this was found in a Raman experiment on a monolayer of FePS<sub>3</sub> [Ref. 4.9]: magnetic Raman peaks are only visible below  $T_N$ . The long-range magnetic order doubles the Brillouin zone, creating new Raman peaks in the antiferromagnetic state.

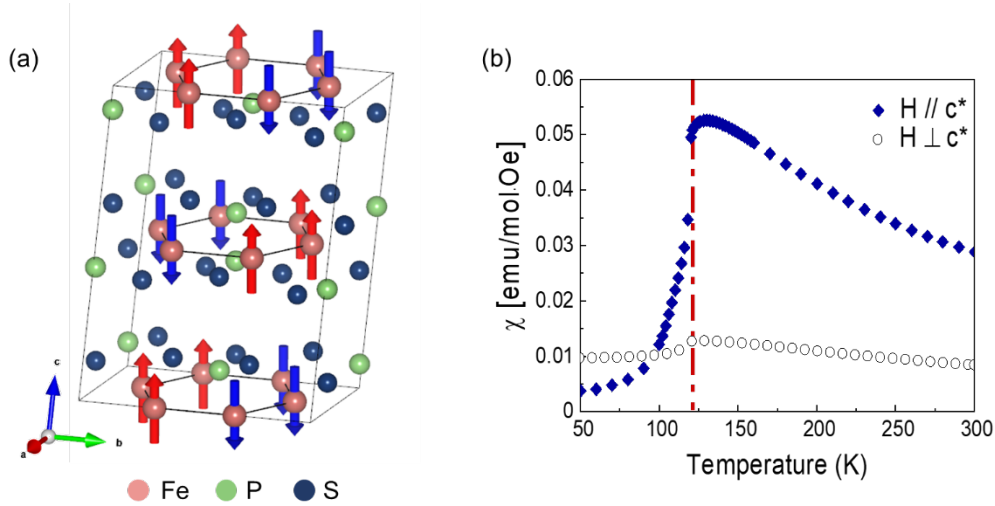


**Figure 4. 1** Ising-type vdW antiferromagnet FePS<sub>3</sub> (a) Schematic of the atomic and magnetic structure of FePS<sub>3</sub>. Pink balls represent Fe<sup>+2</sup> ions which sit on the honeycomb lattice. Spins are ordered parallel to the  $c^*$ -axis, out-of-plane direction, in a zig-zag chain (red and blue arrows). (b) Magnetic susceptibility of bulk FePS<sub>3</sub>.

## 4.3 Methods

### 4.3.1 Sample preparation

To study atomically thin FePS<sub>3</sub>, we mechanically exfoliated a single crystal of FePS<sub>3</sub> to an indium tin oxide (ITO) 70 nm / Si substrate using sticky tape. We used a commercial ITO-coated Si substrate to avoid the charging effect from insulating FePS<sub>3</sub> during the XPEEM experiment. Before the exfoliation, we made Au markers on bare ITO/Si substrate to identify the exfoliated flakes' position. The process of lithography of markers is described in Chapter 3. The thickness of FePS<sub>3</sub> was determined by atomic force microscopy (AFM) measurement. Exfoliation and AFM measurement of flakes were carried out in an argon

gas-filled glove box. Finally, we selected the flake with various thicknesses from monolayer to 20 L, which was appropriate for the thickness dependency study (Figure 4.2 (a, b)).

### 4.3.2 XPEEM experiment

We performed the XPEEM experiment with two linearly polarised x-rays,  $E_{\parallel} = (E, 0, 0)$ , and  $E_{\perp} = (0, E \cdot \sin \theta, E \cdot \cos \theta)$ , and with grazing angle  $\theta = 16^\circ$  being the x-ray's incident angle (Figure 4.2 (c)). The photon energies were from 702 eV to 725 eV, including the Fe  $L_{2,3}$  resonant energies. The temperature range covered the antiferromagnetic to paramagnetic states from 60 to 300 K. To minimise sample degradation from the x-ray exposure, we performed the experiment from low to high temperatures.

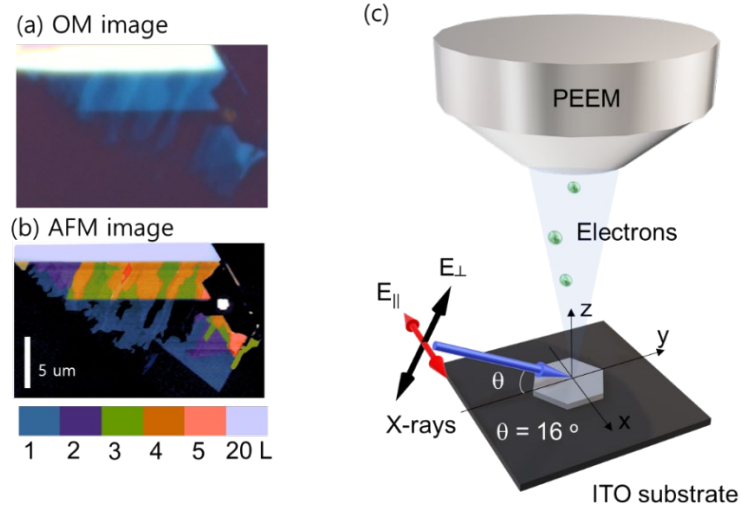


**Figure 4. 2  $\text{FePS}_3$  sample and X-PEEM experiment** Exfoliated few-layer  $\text{FePS}_3$ 's (a) optical microscopic (OM) image and (b) false-colored atomic force microscopy (AFM) image. (c) Schematic image of the PEEM experiment with two linearly polarised x-rays.

## 4.4 Results

### 4.4.1 X-ray absorption spectra

Figure 4.3 shows the X-ray absorption (XA) spectra around the Fe  $L_3$ -edge of 20 L FePS<sub>3</sub> at 65 and 300 K. A linear baseline correction was applied to each spectrum, and each data point was normalised by dividing it by the  $L_3$  peak value. Here, X-ray magnetic linear dichroism (XMLD) is defined as  $I(E_{\perp}) - I(E_{\parallel})$ , where  $I$  is the normalised XA intensity. From the XMLD effect with two orthogonal polarisations ( $E_{\perp}$  and  $E_{\parallel}$ ), we can measure the local antiferromagnetic order.

At 300 K, well above  $T_N$  (the Néel temperature), the XA shows a small but non-zero linear dichroism. This signal reflects a non-magnetic contribution due to the low symmetry of the trigonally distorted FeS<sub>6</sub>. Below  $T_N$ , the long-range magnetic order enhances the linear dichroic signal from the XMLD effect. As we traced the temperature dependence, we observed a significant increase in the amplitude at peaks A, B, and C in both the XA and XMLD spectra with decreasing temperature. The  $X_M$ , the XMLD amplitude of the three peaks A, B, and C, was investigated as a long-range magnetic order parameter. The following multiplet calculation with an exchange field confirmed their relevance to magnetic ordering and magnetic anisotropy.

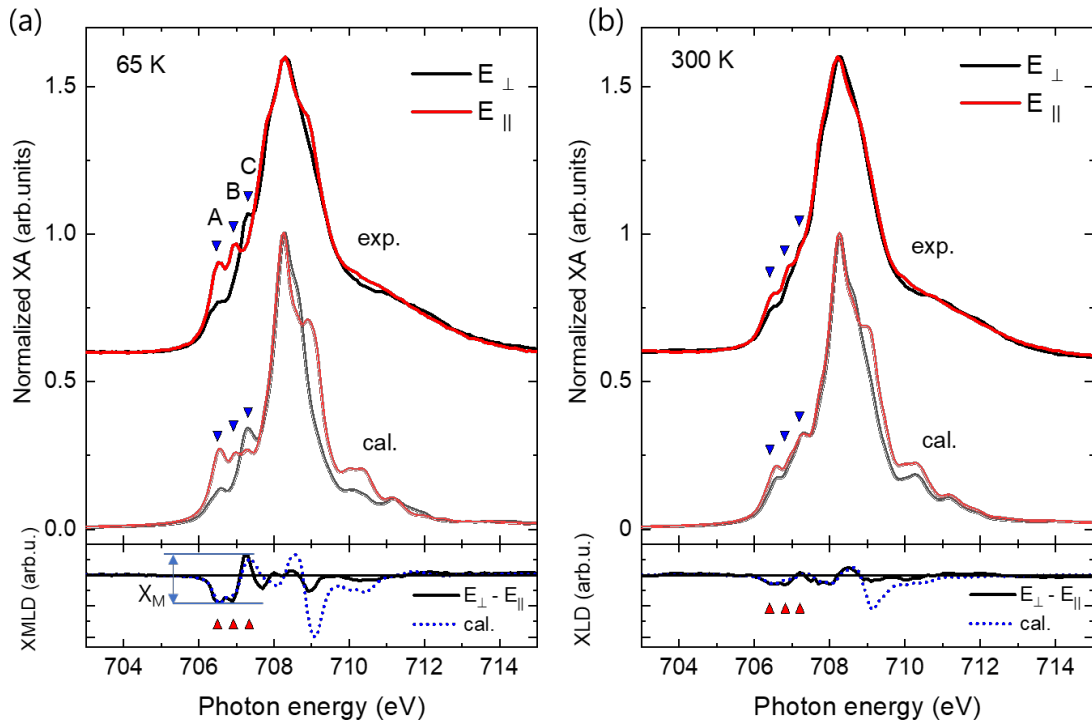


**Figure 4. 3 Temperature-dependent XA spectra** XA spectra in 20 L  $FePS_3$  at **(a)** 65 K and **(b)** 300 K. The experimental (upper) and calculated (lower) XAS are shown. XMLD spectra (bottom) are obtained by the difference between absorption intensity for perpendicular ( $E_{\perp}$ ) and parallel ( $E_{\parallel}$ ) x-ray polarisation.

The physical origins of linear dichroism were investigated using a multiplet calculation that successfully reproduced the experimental spectra. XAS and XMLD spectra were calculated using the Quany code [Ref. 4.10]. We employed a ligand field multiplet model considering the  $pd$ -hybridization of Fe  $d$ -orbitals and S  $p$ -orbitals in the FeS<sub>6</sub> cluster. For the trigonally distorted FeS<sub>6</sub> octahedron, we performed the calculation under the  $D_{3d}$  symmetry. First, we determined the parameters by fitting the XA spectrum at 300 K, excluding the exchange field.

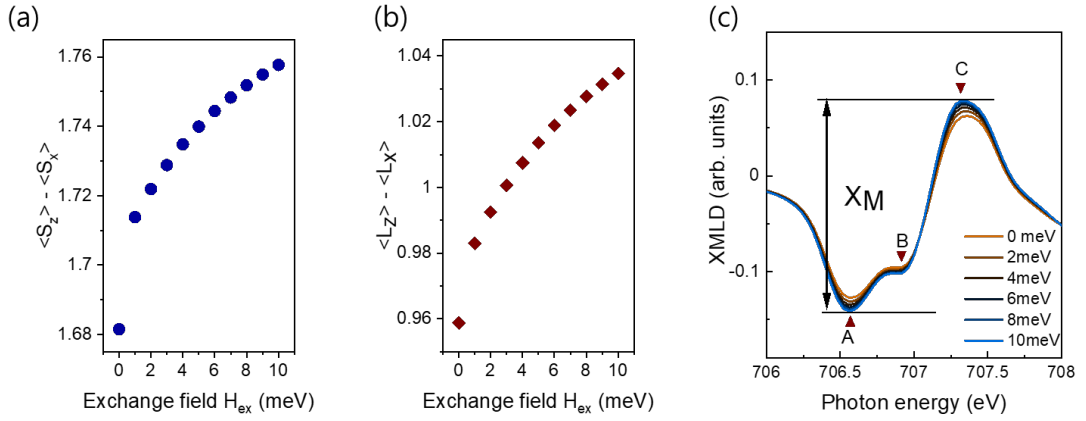


**Figure 4. 4 Exchange field effect on the multiplet simulation.** Anisotropic (a) spin and (b) orbital moment as a function of the applied exchange field  $H_{ex}$ . (c) The XMLD amplitude,  $X_M$ , with various exchange field values.

To reproduce the long-range magnetic order, we introduced an exchange field,  $H_{ex} = \sum_i J \langle S_i \rangle$  that acts only on the spin moment. By applying the exchange field, we could align the spins along the  $z$ -axis (the  $c^*$ -axis in the FePS<sub>3</sub> crystal) (Figure 4.4). Although we applied the exchange field only to the spin, spin-orbit coupling increased the  $z$ -component

of the orbital moment. This increased out-of-plane component of the spin and orbital moments led to a boosted magnetic anisotropy, increasing the XMLD amplitude  $X_M$  (Figure 4.4 (c)). With the long-range magnetic order resulting from the exchange field, we could reproduce the experimental XMLD spectrum at 65 K, where the linear dichroism from the trigonal distortion alone could not explain the amplitude in the antiferromagnetic state (Figure 4.5).

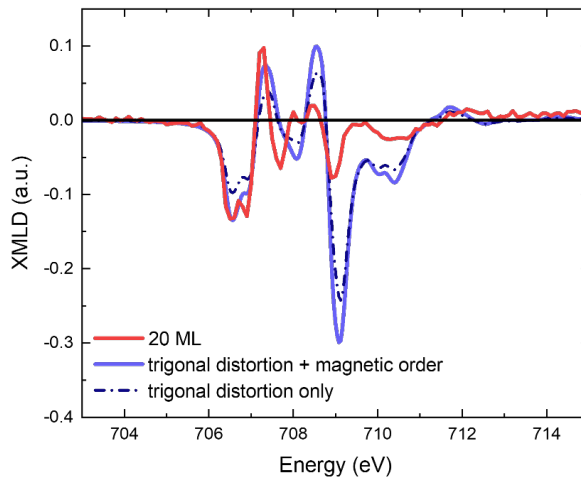


**Figure 4. 5 Reproduction of XMLD spectra at 65 K with the long-range magnetic order in the multiplet calculation.** The solid red line is the experimental 20 L's XMLD spectra. Two simulated XMLD spectra are plotted: the solid purple line results from the combination of trigonal distortion and magnetic ordering via an applied exchange field, and the dotted navy line is that of trigonal distortion alone.

Hamiltonian	Parameters
Atomic terms $H_d$	$U_{dd} = 2.0$ eV $U_{pd} = 2.5$ eV
Crystal field $H_c$	$10Dq = 0.4$ eV $D_{t_{2g}} = -0.01$ eV
Ligand-metal charge transfer $H_{lmet}$	$\Delta = 1.0$ eV $V_{a_{1g}} = 2.3$ eV $V_{e_g\pi} = 2.2$ eV $V_{e_g\sigma} = 3.0$ eV
Ligand crystal field $H_L$	$10Dq^{lig} = 1.5$ eV $D_{t_{2g}}^{lig} = -0.1$ eV

**Table 4. 1. Summary of parameters used for the multiplet simulation**

The Hamiltonian used in Quany is  $H_{tot} = H_d + H_c + H_{lmet} + H_L + H_{ex}$ :

-Atomic terms  $H_d$  refer to the Fe electrons' Coulomb interactions and spin-orbit coupling.

The on-site Coulomb repulsion in different  $d-d$  orbitals  $U_{dd}$

Coulomb interaction between the  $2p$ -core hole and  $3d$ -electron  $U_{pd}$

Slater integrals are reduced to 80% of the Hartree-Fock value with a spin-orbit coupling constant of  $\xi = 0.05$  eV.

- Crystal electric field  $H_c$  reflects the splitting of Fe  $3d$  orbitals by the crystal field

Cubic crystal field  $10Dq$  split Fe  $3d$  orbitals into  $t_{2g}$  and  $e_g$  states.

$D_{t_{2g}}$  is a trigonal distortion parameter that splits the  $t_{2g}$  orbitals into the  $e_g^\pi$  and  $a_{1g}$  states.

$D_{t2g}$  is defined as  $E(e_g^\pi) - E(a_{1g})$ . The negative  $D_{t2g}$  reflects the trigonal elongation, setting the doublet  $e_g^\pi$  as a ground state.

By  $10Dq$  and  $D_{t2g}$ , the energies of the Fe  $3d$  orbitals are described as follows:

$$E_{e_g^\sigma} = 0.6 \times 10Dq \quad (\text{Eq. 4.1})$$

$$E_{a_{1g}} = -0.4 \times 10Dq - 2/3 \times D_{t2g} \quad (\text{Eq. 4.2})$$

$$E_{e_g^\pi} = -0.4 \times 10Dq + 2/3 \times D_{t2g} \quad (\text{Eq. 4.3})$$

- Ligand-metal charge transfer  $H_{\text{lmc}}t$  is the Hamiltonian that considers the charge transfer effect from the S ligand to the Fe  $3d$ -metal.

Charge transfer energy  $\Delta$  is the energy difference between  $d^6$  and  $d^7\bar{L}$ , where  $\bar{L}$  denotes the S  $p$ -orbital hole states;  $\Delta = E(d^7\bar{L}) - E(d^6)$ .

The hopping between the S and Fe ions can be depicted as an effective potential coupling of two different orbitals. This effective potential coupling describes the Fe  $3d$ -orbital energy states of  $D_{3d}$  symmetry: i.e.  $V_{e_g^\sigma}$ ,  $V_{a_{1g}}$ , and  $V_{e_g^\pi}$ .

-  $H_L$  is the sulfur ligand crystal electric field Hamiltonian.

Cubic crystal field parameter  $10Dq^{\text{lig}}$  and trigonal distortion parameter  $D_{t2g}^{\text{lig}}$

#### 4.4.2 Magnetic anisotropy

We employed the Monte-Carlo (MC) simulations and the Bruno model with multiplet calculations to quantify the magnetic anisotropy in FePS<sub>3</sub>. Our analysis revealed a significant magnetic anisotropy due to the interplay between spin-orbit coupling and the crystal field. First, we investigated the magnetic anisotropy through an MC simulation, employing a classical 2D honeycomb lattice Heisenberg exchange model with strong local out-of-plane anisotropy based on the quantum spin Hamiltonian of [Ref. 4.11,4.12]. The Heisenberg exchange coupling includes up to the fourth nearest neighbor. We considered only intralayer exchange interactions, following [Ref. 4.12], because including an interlayer exchange interaction as in [Ref. 4.11] resulted in a minor change.

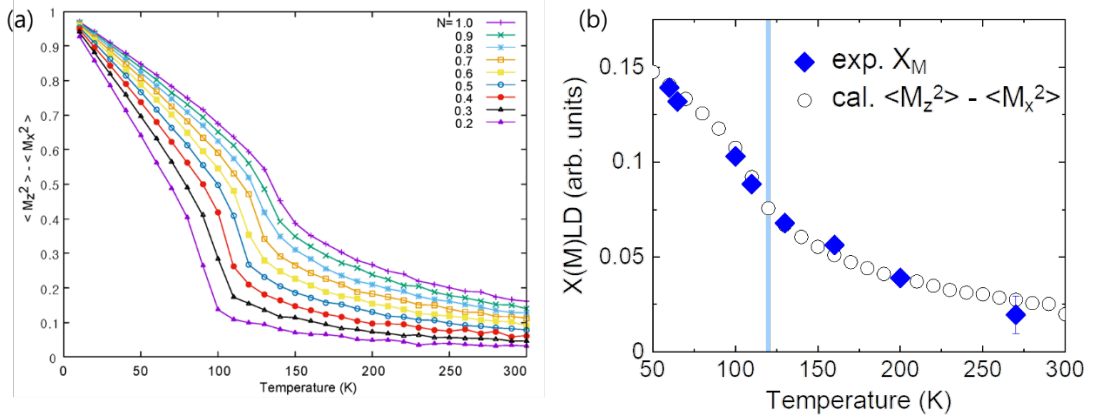


**Figure 4. 6 Magnetic anisotropies from the MC simulation** (a) MC simulated quantity  $\langle M_z^2 \rangle - \langle M_x^2 \rangle$  with fixed exchange parameter  $J$  and different magnetic anisotropy  $K_N = K \cdot N$ ,  $K = 26.6$  meV. (b) Experimental XMLD amplitude  $X_M$  (blue diamond) together with  $\langle M_z^2 \rangle - \langle M_x^2 \rangle$  from the MC calculation (white circle) for 20 L FePS<sub>3</sub> as a function of temperature.

Thus, our classical vdW material is modelled as a stack of noninteracting MLs, each described by the equation,

$$H = -\frac{1}{2} \sum_{ij} J_{ij} \hat{m}_i \cdot \hat{m}_j - K \sum_i (\hat{m}_{z,i})^2 \quad (\text{Eq. 4.4})$$

The adopted exchange parameters  $J_1 = 14.6$ ,  $J_2 = -0.4$ ,  $J_3 = -9.6$  and  $J_4 = -0.073$  meV and an out-of-plane anisotropy  $K = 22$  meV reproduced the Néel temperature of 115 K. Based on the Hamiltonian, we calculated the  $\langle M_z^2 \rangle - \langle M_x^2 \rangle$  and compared it to the experimental  $X_M$  value as a function of temperature (Figure 4. 6 (b)). The temperature-dependent  $X_M$  coincides with  $\langle M_z^2 \rangle - \langle M_x^2 \rangle$  from MC simulation with the single-ion anisotropy  $K$ , which estimated the magnetic anisotropy in 20 L FePS<sub>3</sub> as 22 meV / Fe.

Using the perturbation treatment, Bruno verified that magnetic anisotropy is related to the spin-orbit interaction [Ref. 4.13]. This relation can be quantified as  $\frac{1}{4} \xi \hat{S} \cdot (\Delta L)$ , where  $\Delta L$  is the orbital momentum difference between the easy axis and hard axes [Ref. 4.14,4.15]. From the equation, we obtained the magnetic anisotropy where for the present case, the orbital moment anisotropy  $\Delta L = (L_z - L_x)$  and spin moment  $S$  were obtained from the multiplet calculations by fitting the respective XA spectra at 65 K. Here,  $\xi$  is an atomic spin-orbit coupling constant with a value of 50 meV for Fe<sup>+2</sup>. The multiplet calculation gives the expectation value of the spin and orbital moments: spin moment  $\langle S_z \rangle = 1.75$  and orbital moment  $\langle L_z \rangle = 1.02$  per Fe ion. These values are comparable to those of Fe<sup>+2</sup> ions in a d<sup>6</sup> high spin state with unquenched  $S = 2$  and  $\tilde{L} = 1$ . This unquenched magnetic orbital moment originated from the reduced symmetry by the trigonal distortion of the FeS<sub>6</sub> octahedron [Ref. 4.16]. Using Bruno's model, we obtained a magnetic

anisotropy value of about 22 meV / Fe, which is the same as the MC calculation.

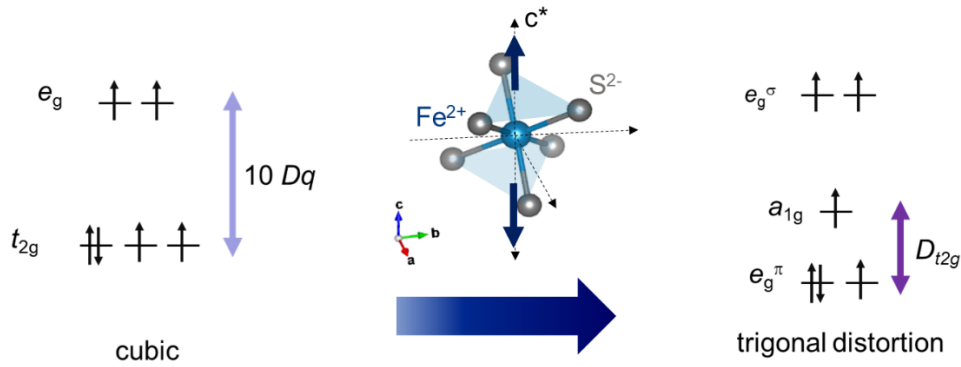


**Figure 4. 7 Trigonal elongation and corresponding orbital splitting in FePS<sub>3</sub>.**

We note that the XMCD and XMLD techniques were previously employed to investigate the Ising metallic ferromagnetic system Fe<sub>1/4</sub>TaS<sub>2</sub> [Ref. 4.15] which, like FePS<sub>3</sub>, has high magnetic anisotropy, 14 meV/Fe, due to the interaction of unquenched orbital moments caused by poor symmetry and spin-orbit coupling

It is also interesting to compare other vdW Ising-type magnets CrI<sub>3</sub> with FePS<sub>3</sub>. CrI<sub>3</sub> monolayer is an Ising ferromagnet with Curie temperature ( $T_c$ ) of 45 K [Ref. 4.17]. As in the FePS<sub>3</sub>, the monolayer CrI<sub>3</sub> exhibits a long-range magnetic order [Ref. 4.17,4.18], and it has a small magnetic anisotropy of only 0.65 meV [Ref. 4.19]. This value can be attributed to two factors: (i) anisotropic super-exchange across Cr-I-Cr with the spin-orbit interaction of the ligand I atoms and (ii) single ion anisotropy from the Cr atom. The single ion anisotropy of the Cr atom is much smaller than the anisotropic super-exchange contribution. The Cr<sup>+3</sup> ions in a  $d^3$  high spin state with high crystal symmetry exhibit a

quenched orbital moment, resulting in the small single-ion anisotropy value.

### 4.4.3 XMLD asymmetric images

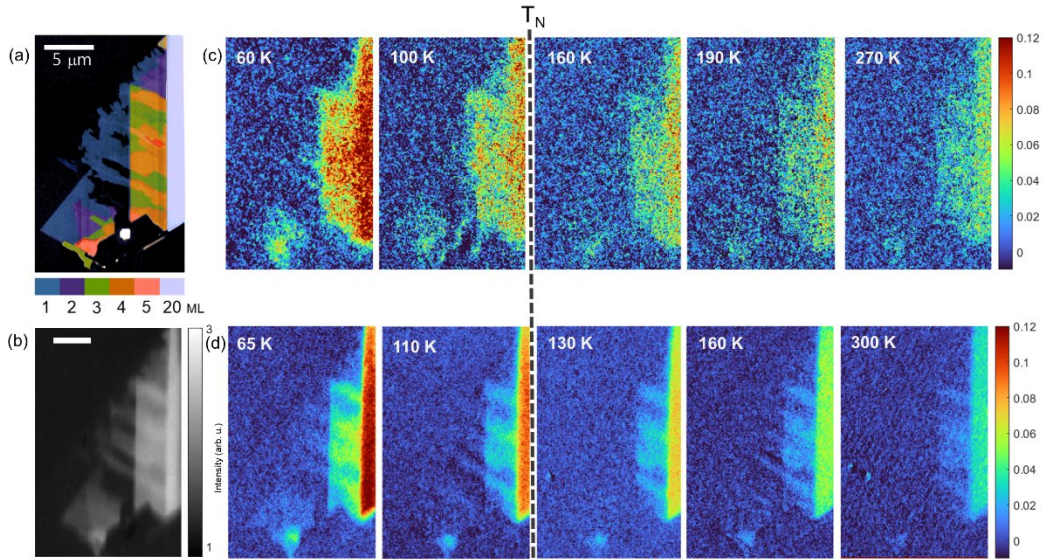


**Figure 4. 8 XMLD asymmetric map** (a) False colored AFM image (b) Normalised X-PEEM images. XMLD asymmetric images in the (c) first and (d) second thermal cycle. The larger averaging number of XPEEM images in the second thermal cycle produced higher resolution and lower noise levels compared to the first cycle.

The local magnetic order of the FePS<sub>3</sub> flake is visualised using an XMLD contrast map. The XMLD contrast map was obtained through pixel-wise evaluation of the normalised XMLD asymmetry  $A = \left[ I_{\perp}^{(C,B)} - I_{\parallel}^{(C,B)} \right] / \left[ I_{\perp}^{(C,B)} + I_{\parallel}^{(C,B)} \right]$ , where  $I^{(C,B)}$  denotes the intensity ratio of peaks C and B,  $I(C) / I(B)$ . This evaluation method was used for lower noise in XMLD images. From the XMLD contrast map, the monolayer's XMLD signal at

low temperatures could be observed. The high sensitivity of the XMLD contrast map to the XMLD signal enabled the observation of long-range magnetic order in the monolayer.

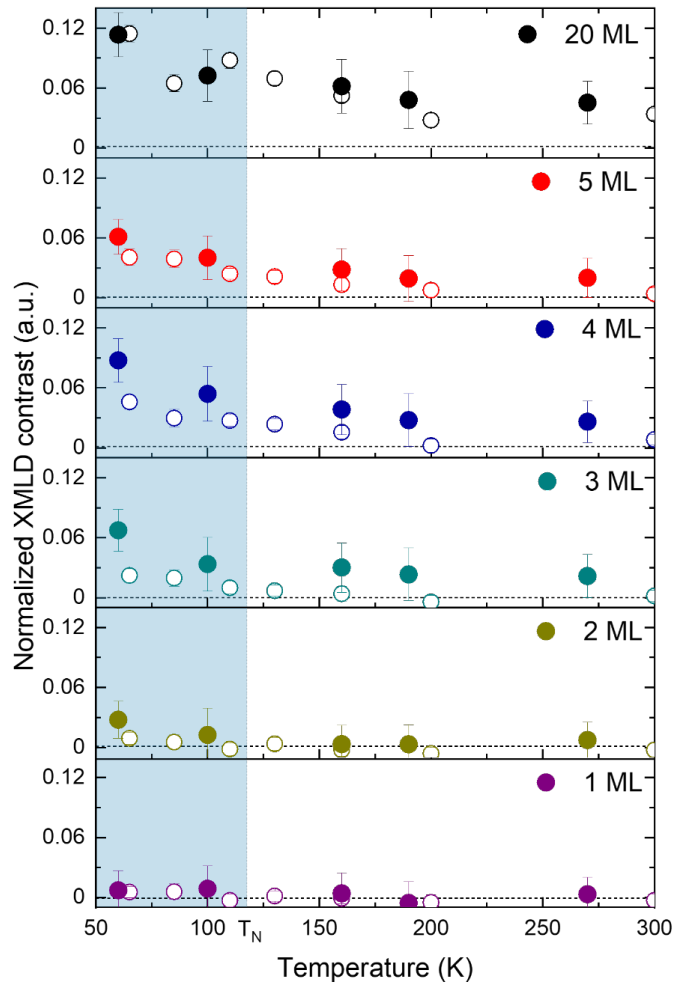


**Figure 4.9 Normalised XMLD contrast value  $A$  from the XMLD asymmetric map**  
 Filled circles are values obtained from the first scan, while the vacant circles are from the second scan's contrast amplitude.

#### 4.4.4 Thickness dependency

As the number of layers decreased, a reduction in the XMLD amplitude of the asymmetric XMLD map was observed. This decrease in XMLD amplitude with thinner FePS<sub>3</sub> was also reflected in the XMLD spectra (Figure 4. 10).

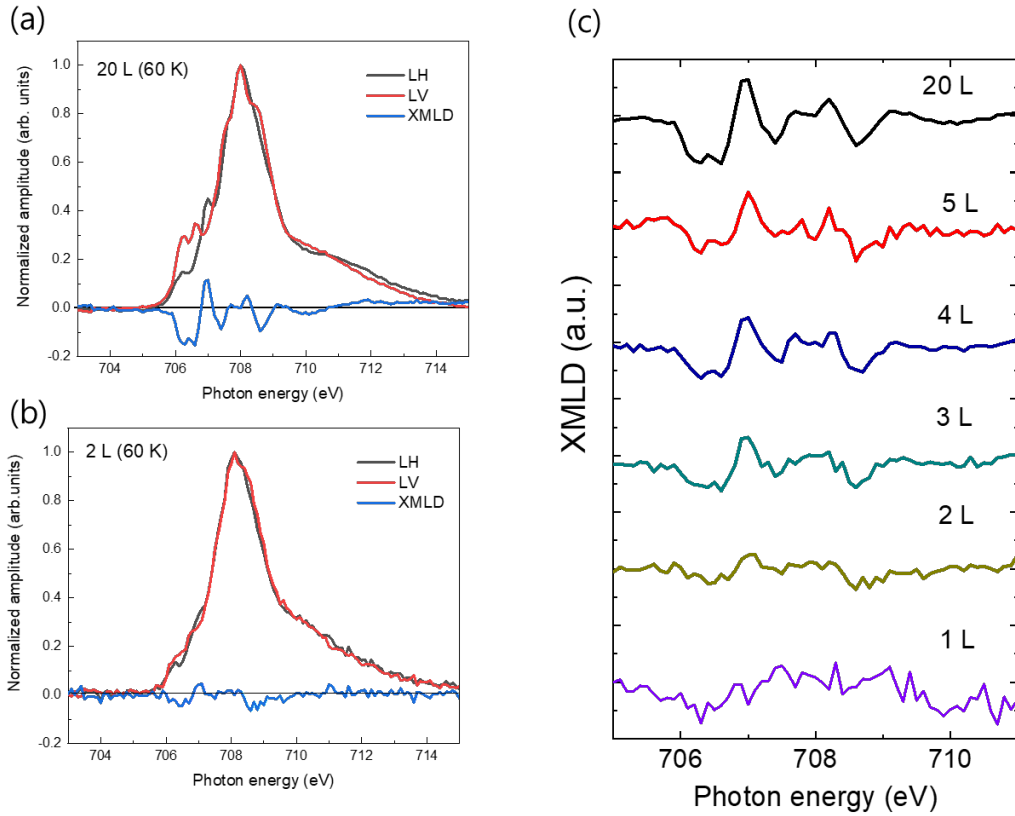


**Figure 4. 10** Thickness-dependent XA and XMLD spectra XA and XMLD spectra in (a) 20 L and (b) 2 L at 60 K. (c) Thickness-dependent XMLD spectra from 20 L to 1 L.

We calculated the magnetic anisotropy as a function of thickness using the method mentioned above for the case of 20 L. First, we extracted the magnetic anisotropy for thicknesses down to 3 L by fitting the experimental  $X_M$  data to the simulated  $\langle M_z^2 \rangle - \langle M_x^2 \rangle$

from the MC simulation of different magnetic anisotropy  $K_N$  (Figure 4. 11). The results showed that for thicknesses down to 4 L, the anisotropy value remained constant with that of the 20 L sample, but for 3 L, the anisotropy value was estimated to be half that of the 20 L sample. However, it was challenging to fit the experimental data  $X_M$  with the simulated  $\langle M_z^2 \rangle - \langle M_x^2 \rangle$  as a function of temperature for thicknesses from 2 L to 1 L as the experimental values decreased rapidly to zero with temperature (Figure 4. 9). We could deduce that the thinner samples were more sensitive to the x-ray exposure, leading to rapid degradation of the experimental data in thinner layers.

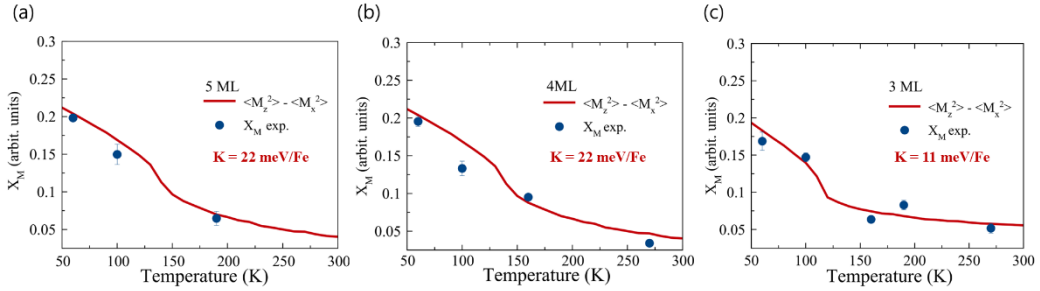


**Figure 4. 11** Temperature-dependent  $\langle M_z^2 \rangle - \langle M_x^2 \rangle$  and  $X_M$  in few-layer FePS<sub>3</sub> Fitting experimental data  $X_M$  with the simulated  $\langle M_z^2 \rangle - \langle M_x^2 \rangle$  from the MC simulation of different magnetic anisotropy  $K_N$  in (a) 5 L, (b) 4 L, and (c) 3 L.

The Bruno model calculation also allows us to estimate the magnetic anisotropy even in the monolayer of FePS<sub>3</sub>. Using this method with multiplet calculation, we extracted the required spin and orbital moment from the XA at 60 K and obtained the magnetic anisotropy value for the monolayer. We comment that the Bruno model yielded the same

result as the MC calculation down to 4 L, but the value for 3 L was 20.6 meV/Fe, showing a slight decline in magnetic anisotropy. This decrease was compared with the drop in the MC calculation's result, suggesting that the inconsistency could be due to the degradation of the three layers of the sample during the temperature experiment. While the magnetic anisotropy value obtained from the MC method reflected this degradation, the value obtained from Bruno's model method did not.

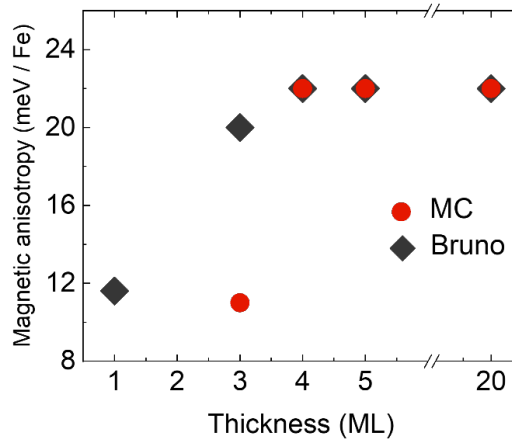


**Figure 4. 12 Magnetic anisotropy as a function of thickness extracted from MC simulation (red circles) and Bruno's model (grey diamonds).**

The magnetic anisotropy value of the monolayer was 11.6 meV/Fe, which is half that of 20 L. This decrease was caused by charge transfer from the ITO substrate. The work function mismatch between the p-type semiconductor FePS<sub>3</sub> [Ref. 4.20,4.21] and metallic ITO substrate [Ref. 4.22] led to electron transfer from ITO to FePS<sub>3</sub>. This interfacial charge

transfer effect resulted in a different spectrum for the monolayer compared to that of 20 L (Figure 4. 13). The monolayer had a higher intensity in the shoulder around 710 eV after the  $L_3$  resonance peak and reduced intensities in peaks A, B and C (Figure 4. 13 (a)).

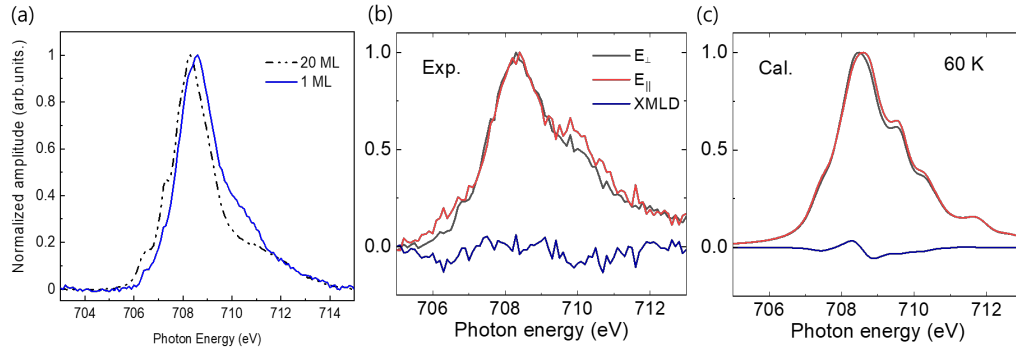


**Figure 4. 13 Substrate effect on the 1 L.** (a) 1L XA spectrum deviated from the 20 L XA spectrum. The 1L XA and XMLD spectra at 60 K of (b) experiment and (c) multiplet simulation with different parameters.

Hamiltonian	Parameters
Ligand-metal charge transfer $H_{lmct}$	$\Delta = -6.0$ eV $V_{a1g} = 1.5$ eV $V_{eg\pi} = 1.5$ eV $V_{eg\sigma} = 2.0$ eV
Ligand crystal field $H_L$	$10Dq^{lig} = 0$ eV $D_{t2g}^{lig} = 0$ eV

**Table 4. 2. Modified parameters for monolayer's multiplet simulation.**

We calculated the monolayer's XA spectra with different parameters in the multiplet simulation to reproduce the XA spectra and verify the charge transfer effect. We reduced the value of the charge transfer energy  $\Delta$  and the effective coupling potentials  $V_{alg}$ ,  $V_{eg\pi}$ ,  $V_{eg\sigma}$  to reflect the electron transfer from the substrate (Table 4. 2) while keeping the other parameters the same as those of the 20 L. The simulation with modified parameters reproduced the changes in the XA spectra for the monolayer (Figure 4. 13 ©). The  $3d$  electron occupation number from the simulation was  $\langle N_{3d} \rangle = 6.77$  for the monolayer, while the bulk value was found to be  $\langle N_{3d} \rangle = 6.38$ . This yielded the decreased  $\langle S_z \rangle = 1.29$  and  $\langle L_z \rangle = 0.42$ , resulting in the reduced magnetic anisotropy determined by Bruno's model.

We probed the presence of the long-range magnetic order with reduced magnetic anisotropy in the monolayer from the XMLD asymmetric image and multiplet simulation with modified parameters. To confirm this, we measured the monolayer's Raman spectrum on the ITO substrate using a laser with a wavelength of 488 nm and a power of  $\sim 50 \mu\text{W}$  in an optical cryostat. The scattered light from the sample was dispersed using a Jobin-Yvon Horiba iHR550 spectrometer (2400 grooves/mm) and detected with a liquid nitrogen-cooled CCD. We observed the  $P_1$  and  $P_2$  peaks down to the monolayer, which were only observable in the antiferromagnetic state (Figure 4.14), consistent with our conclusion in the XPEEM experiment.

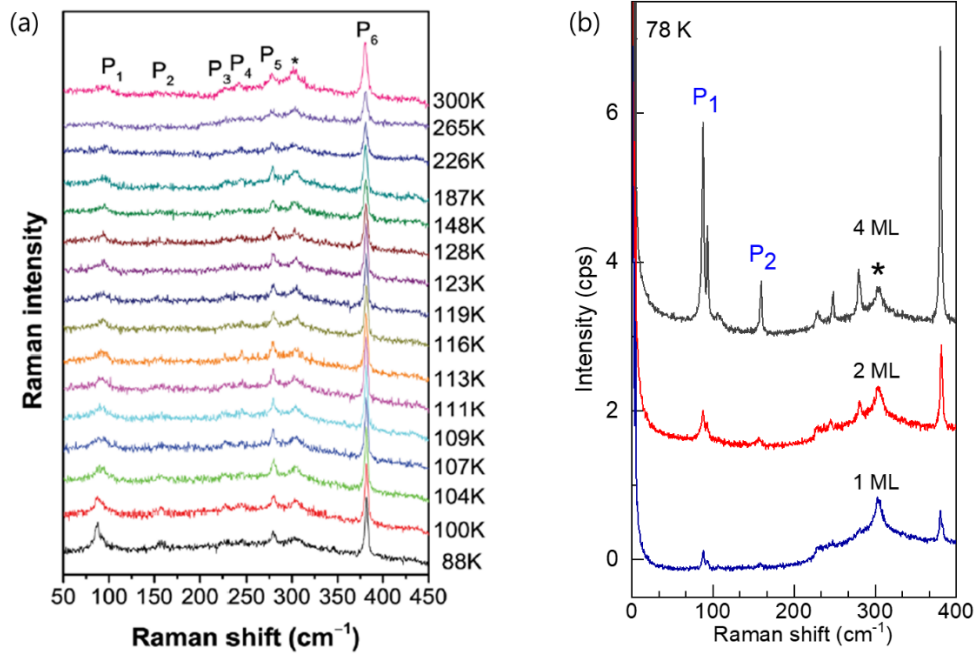


**Figure 4. 14 Raman shift in few-layer  $\text{FePS}_3$**  (a) 1 L  $\text{FePS}_3$ 's Raman spectrum on Si substrate [Ref. 4.7] (b) Raman spectrum on ITO/Si substrate. The peaks marked with an asterisk were signals of Si and ITO/Si substrates, respectively.

## 4.5 Summary

We investigated the spontaneous antiferromagnetic order in the van der Waals Ising antiferromagnet  $\text{FePS}_3$  at the atomic limit, using the sensitivity and high spatial resolution of X-PEEM combined with XMLD (XMLD-PEEM) to probe the magnetism. The resulting magnetic anisotropy value from the single-ion anisotropy was estimated to be 22 meV per Fe ion. The large magnetic anisotropy stemmed from the low symmetry of the  $\text{FeS}_6$  cluster and the spin-orbit coupling effect. This magnetic anisotropy was preserved or slightly

reduced to the tri-layer, and the monolayer had only half of the bulk value. The charge transfer from the metallic substrate to FePS<sub>3</sub> changed the electronic configuration in FePS<sub>3</sub>, which we think reduced the orbital moments and the magnetic anisotropy. Although the magnetic anisotropy decreased, the long-range antiferromagnetic order still existed in the monolayer, which was confirmed by observing the monolayer's XMLD signal in the XMLD asymmetric image.

## References

- [Ref. 4.1] Mermin, N. D. and Wagner, H. *Phys. Rev. Lett.* **17**, 1133, (1966).
- [Ref. 4.2] Afanasiev, D., Hortensius, J. R., Matthiesen, M., Mañas-Valero, S., Šiškins, M., Lee, M., Lesne, E., van Der Zant, H. S. J., Steeneken, P. G., and Ivanov, B. A. *Science Advances* **7**, eabf3096, (2021).
- [Ref. 4.3] Deng, Y., Yu, Y., Song, Y., Zhang, J., Wang, N. Z., Sun, Z., Yi, Y., Wu, Y. Z., Wu, S., and Zhu, J. *Nature* **563**, 94-99, (2018).
- [Ref. 4.4] Ni, Z., Haglund, A. V., Wang, H., Xu, B., Bernhard, C., Mandrus, D. G., Qian, X., Mele, E. J., Kane, C. L., and Wu, L. *Nature Nanotechnology* **16**, 782-787, (2021).
- [Ref. 4.5] Tang, M., Huang, J., Qin, F., Zhai, K., Ideue, T., Li, Z., Meng, F., Nie, A., Wu, L., Bi, X., Zhang, C., Zhou, L., Chen, P., Qiu, C., Tang, P., Zhang, H., Wan, X., Wang, L., Liu, Z., Tian, Y., Iwasa, Y., and Yuan, H. *Nature Electronics* **6**, 28-36, (2023).
- [Ref. 4.6] Rau, I. G., Baumann, S., Rusponi, S., Donati, F., Stepanow, S., Gagnaniello, L., Dreiser,

- J., Piamonteze, C., Nolting, F., and Gangopadhyay, S. *Science* **344**, 988-992, (2014).
- [Ref. 4.7] Lee, J.-U., Lee, S., Ryoo, J. H., Kang, S., Kim, T. Y., Kim, P., Park, C.-H., Park, J.-G., and Cheong, H. *Nano Letters* **16**, 7433-7438, (2016).
- [Ref. 4.8] Onsager, L. *Phys. Rev.* **65**, 117-149, (1944).
- [Ref. 4.9] Lee, J. U., Lee, S., Ryoo, J. H., Kang, S., Kim, T. Y., Kim, P., Park, C. H., Park, J. G., and Cheong, H. *Nano Lett.* **16**, 7433-7438, (2016).
- [Ref. 4.10] Haverkort, M. W., Zwierzycki, M., and Andersen, O. K. *Phys. Rev. B* **85**, 165113, (2012).
- [Ref. 4.11] Lançon, D., Walker, H. C., Ressouche, E., Ouladdiaf, B., Rule, K. C., McIntyre, G. J., Hicks, T. J., Rønnow, H. M., and Wildes, A. R. *Phys. Rev. B* **94**, 214407, (2016).
- [Ref. 4.12] Wildes, A. R., Rule, K. C., Bewley, R. I., Enderle, M., and Hicks, T. J. *J. Phys. Condens. Matter* **24**, 416004, (2012).
- [Ref. 4.13] Bruno, P. *Phys. Rev. B* **39**, 865, (1989).
- [Ref. 4.14] van der Laan, G. *Journal of Physics: Condensed Matter* **10**, 3239, (1998).
- [Ref. 4.15] Ko, K.-T., Kim, K., Kim, S. B., Kim, H.-D., Kim, J.-Y., Min, B., Park, J.-H., Chang, F.-H., Lin, H.-J., and Tanaka, A. *Phys. Rev. Lett.* **107**, 247201, (2011).
- [Ref. 4.16] Joy, P. A. and Vasudevan, S. *Phys. Rev. B* **46**, 5425-5433, (1992).
- [Ref. 4.17] Huang, B., Clark, G., Navarro-Moratalla, E., Klein, D. R., Cheng, R., Seyler, K. L., Zhong, D., Schmidgall, E., McGuire, M. A., Cobden, D. H., Yao, W., Xiao, D., Jarillo-Herrero, P., and Xu, X. *Nature* **546**, 270-273, (2017).
- [Ref. 4.18] Thiel, L., Wang, Z., Tschudin, M. A., Rohner, D., Gutiérrez-Lezama, I., Ubrig, N., Gibertini, M., Giannini, E., Morpurgo, A. F., and Maletinsky, P. *Science* **364**, 973-976, (2019).

#### ***Chapter 4 Large magnetic anisotropy in FePS<sub>3</sub>***

---

- [Ref. 4.19] Lado, J. L. and Fernández-Rossier, J. *2D Materials* **4**, 035002, (2017).
- [Ref. 4.20] Aruchamy, A., Berger, H., and Levy, F. *J. Solid State Chem.* **72**, 316-323, (1988).
- [Ref. 4.21] Zhang, X., Zhao, X., Wu, D., Jing, Y., and Zhou, Z. *Adv. Sci.* **3**, 1600062, (2016).
- [Ref. 4.22] Park, Y., Choong, V., Gao, Y., Hsieh, B. R., and Tang, C. W. *Appl. Phys. Lett.* **68**, 2699-2701, (1996).

## **Chapter 5**

# **Magnetic domains and their thermal fluctuations in vdW antiferromagnet NiPS<sub>3</sub>**

### **5.1 Introduction**

The mechanism of antiferromagnetic (AF) domains is ambiguous compared with that of ferromagnets. The primary origin of the AF domain is the competition between a single magnetic anisotropy and exchange interaction. It is also important to note the role of magnetostriction, where AF domains are formed to minimise the strain caused by magnetostriction. In epitaxial films, one of the origins of multidomain formation is the strain from the substrate induced by the magnetoelastic effect [Ref. 5.1]. Van der Waals (vdW) materials have relatively weaker interactions with the substrate than epitaxial thin films. Therefore, we expect a different mechanism for domain formation in vdW antiferromagnets. In this study, we investigate the magnetic domains in vdW antiferromagnet NiPS<sub>3</sub> using PEEM with linearly polarised X-rays. We observed clear thermal fluctuations in the domains and discovered that the primary mechanism in the multidomain structure was weak magnetic anisotropy in NiPS<sub>3</sub>.

#### **5.1.1 Magnetic domains in TMPX<sub>3</sub>**

Few studies have been conducted on the magnetic domains in vdW antiferromagnets, particularly in the TMPX<sub>3</sub> family (TM = Mn, Fe, and Ni; X = Se and S). The domains in Néel-type antiferromagnets MnPSe<sub>3</sub> and MnPS<sub>3</sub> were observed using the second harmonic generation (SHG) technique [Ref. 5.2,5.3]. The broken inversion symmetry in the Néel-

type antiferromagnets allowed the two antiphase magnetic domains to be investigated based on the SHG (Figure 5. 1(a)). In principle, SHGs are not allowed in the centrosymmetric zigzag-ordered antiferromagnet FePS<sub>3</sub>, whereas the broken inversion symmetry on the surface enables SHG analysis in a few-layer FePS<sub>3</sub> [Ref. 5.4]. In the polarisation-dependent SHG and linear dichroism (LD) measurements with spatial resolution, three magnetic domains with zigzag directions 120° to each other were observed in a three-layer FePS<sub>3</sub> flake (Figure 5. 1(b)). Another study investigated the magnetic domains in FePS<sub>3</sub> with polarisation-dependent optical LD [Ref. 5.5]. The angle-dependent LD showed a 60°-rotated zigzag chain direction in the FePS<sub>3</sub> flake. For NiPS<sub>3</sub>, its magnetic domains were analysed using an anisotropic exciton coupled with a Néel vector [Ref. 5.6]. In polarisation-resolved PL measurements, exfoliated NiPS<sub>3</sub> flakes with different thicknesses exhibited distinct maximal photoluminescence (PL) intensity directions. The polarisation-resolved PL showed three magnetic domains with a rotating angle of 120° from each other.

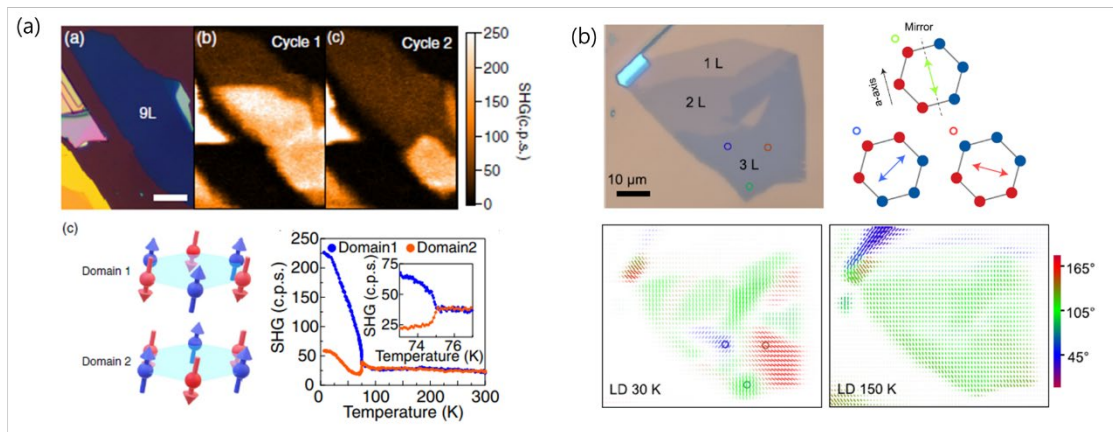


**Figure 5. 1 Observation of antiferromagnetic domains in TMPS<sub>3</sub> via optical techniques.** (a) Two antiphase domains in MnPS<sub>3</sub> [Ref. 5.3]. (b) Three different spin chain domains in FePS<sub>3</sub> [Ref. 5.4]

### 5.1.2 vdW antiferromagnet NiPS<sub>3</sub>

The Ni atoms are arranged in a honeycomb lattice, and one Ni atom is surrounded by six S atoms, thus forming a NiS<sub>6</sub> octahedron. The NiS<sub>6</sub> octahedron is trigonally compressed, whereas the FeS<sub>6</sub> in FePS<sub>3</sub> is trigonally elongated [Ref. 5.7]. Monolayer NiPS<sub>3</sub> exhibits a three-fold rotational symmetry; however, the symmetry in the multilayer is broken owing to monoclinic stacking, which induces easy-axis anisotropy along the *a*-axis. Thus, the spins are aligned along the *a*-axis and tilt slightly along the *c*-axis in the antiferromagnetic state [Ref. 5.8]. Each ferromagnetic chain exhibits net magnetisations  $M_1$  and  $M_2$ , and the Néel vector  $L$  can be defined as  $L = M_1 - M_2$ . Both  $M_1$  and  $M_2$  are parallel to the *a*-axis; therefore, the Néel vector  $L$  is parallel to the *a*-axis. The phase transition from paramagnetic to antiferromagnetic occurred at approximately 155 K, the highest temperature reported for TMPS<sub>3</sub> (TM = Mn, Ni, and Fe).

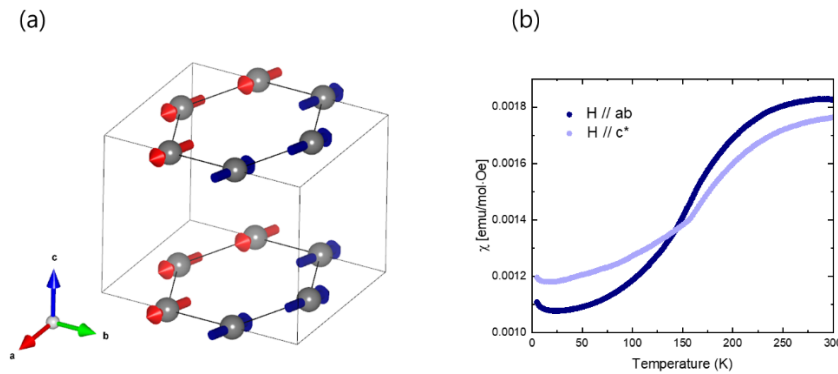


**Figure 5. 2 (a) Magnetic structure and (b) magnetic susceptibility of NiPS<sub>3</sub>.** The magnetic susceptibility of bulk NiPS<sub>3</sub> was measured using a commercial magnetometer (MPMS-XL5, Quantum Design). The measurement was performed via field cooling under a 300 Oe magnetic field.

NiPS<sub>3</sub> hosts a magnetic exciton that couples to its antiferromagnetic state [Ref. 5.9,5.10,5.11]. Using multiple spectroscopic probes, the observed excitons were assigned to the transition from the Zhang–Rice triplet to a singlet [Ref. 5.9]. The ultra-narrow and sharp PL peaks implied coherent excitation. The magnetic exciton was anisotropic with respect to the Néel vector and indicated polarisation dependency on the PL and optical dichroism at the exciton resonance energy. The strong correlation between the exciton and the Néel vector highlights the necessity to understand the dynamics of the Néel vector in NiPS<sub>3</sub> magneto-optical devices.

## **5.2 Methods**

The sample preparation and experimental methods were similar to those for the FePS<sub>3</sub> PEEM experiments. We used a conducting indium tin oxide (ITO coated Si substrate to reduce the charging problem from the insulating NiPS<sub>3</sub>. The gold markers with numbers were patterned with conventional photolithography. Then single crystal NiPS<sub>3</sub> was exfoliated on the substrate by mechanical method.

We used two linearly polarised x-rays,  $E_{\parallel} = (E, 0, 0)$ , and  $E_{\perp} = (0, E \cdot \sin\theta, E \cdot \cos\theta)$ , and with grazing angle  $\theta = 16^{\circ}$  being the x-ray's incident angle. The absorption intensities were measured in electron-yield mode and the incident photon energy was adjusted to accommodate the Ni  $L_3$  edge (845–870 eV). The temperature range was from 60 to 285 K, including the Néel temperature, 155 K.

## **5.3 Results**

### **5.3.1 Observation of magnetic domain**

We observed the magnetic domains in the asymmetric XMLD images (Figure 5.3 (b)). The asymmetric XMLD image was calculated pixel-wise using the expression  $(I_{\parallel} - I_{\perp}) / (I_{\parallel} + I_{\perp})$

with an incident photon energy of 850.2 eV, the resonant energy of the XMLD peak. The observed region was flat, as confirmed via atomic force microscopy (AFM) measurements. Except for the dotted grey line in the OM image and the normalised XPEEM image, the region of interest was 48 nm thick (Figures 5.3 (a) and (c)). We measured the X-PEEM images using two circularly polarised X-rays (C<sup>+</sup> and C<sup>-</sup>) to investigate the domain walls. The uncompressed magnetisation in the domain wall [Ref. 5.12] can provide an XMCD signal. The asymmetric XMCD image was calculated using the expression  $(C^+ - C^-)/(C^+ + C^-)$ , and we could not identify the XMCD signal from the domain wall. This implies that the domain-wall size should be smaller than the spatial resolution of XPEEM, i.e. 45 nm.

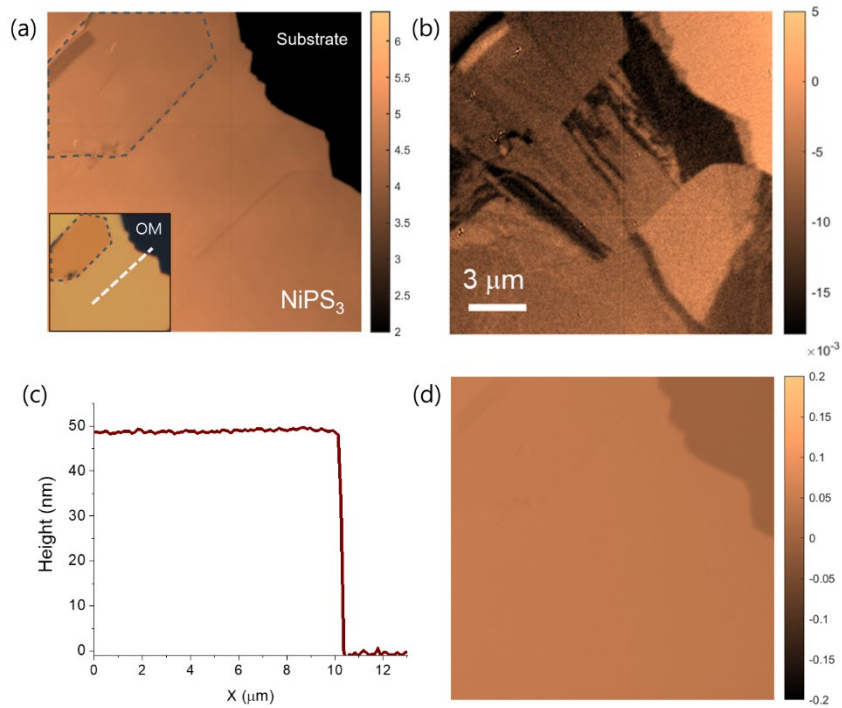


**Figure 5. 3 Magnetic domains in NiPS<sub>3</sub>** (a) X-PEEM elemental contrast map of exfoliated NiPS<sub>3</sub> flake. The area presented in copper shows NiPS<sub>3</sub> flake, and the black region in the right-upper region shows the substrate. Inset shows an OM image of the sample. (b)

Corresponding XMLD asymmetric map calculated pixel-wise using the expression  $(I_{\parallel} - I_{\perp})/(I_{\parallel} + I_{\perp})$ . (c) AFM profile along the white line in the OM image in (a). (d) XMCD asymmetric map. Images in (a), (b), and (d) were obtained with a photon energy of 850.2 eV at 70 K (a, b) and 68 K (d).

### 5.3.2 Temperature dependence of magnetic domain

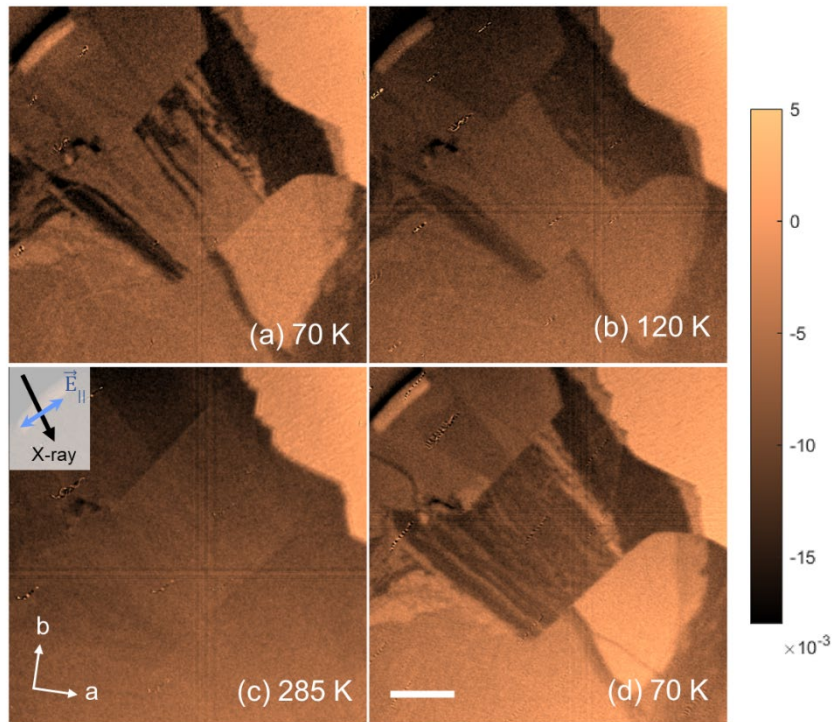


**Figure 5. 4 Temperature dependence on the magnetic domains.** NiPS<sub>3</sub> sample was cooled below  $T_N$  (a, b) and then heated to a high temperature above  $T_N$ . Subsequently, it was cooled again at a different cooling rate compared with that of the first thermal cycle (d).

We investigated the temperature dependence to confirm the magnetic origin of the domains. The effect of the magnetic order on the XMLD effect indicated a significant temperature dependence, whereas the XNLD signal from the anisotropic orbital indicated minimal

dependence on temperature [Ref. 5.13]. The XMLD contrast was clearly observed at 70 K, decreased with increasing temperature, and almost vanished above the Néel temperature (Figures 5.4 (a–c)). The remaining slight contrast at 285 K might have originated from the short-range magnetic order [Ref. 5.3]. The spin–spin correlation is typically disregarded in XMLD intensities because of its minimal contribution compared with the long-range antiferromagnetic order; however, it can provide a non-zero contribution. The magnetic susceptibility of bulk NiPS<sub>3</sub> showed an overall decrease even in the paramagnetic state, thus indicating the presence of a short-range magnetic order (Figure 5. 2 (b)). Further evidence for the magnetic domain is the different domain morphologies at different cooling rates. When the temperature decreased to 70 K, the magnetic domain contrast was reproduced with a smaller domain size (Figure 5. 4 (d)). The domains shown in Figure 5. 4 (a) had a cooling rate of 1.25 K/min, whereas that shown in Figure 5. 4 (d) cooled more rapidly at a cooling rate of 4.9 K/min. The low cooling rate and sufficient relaxation time for the domain growth resulted in the formation of large domains.

The experimental geometry, including the X-ray propagation direction with the in-plane electric field polarisation and crystalline axes, is shown in Figure 5. 4 (c). The crystalline *a*- and *b*-axes were determined via polarisation-dependent Raman spectroscopy (Figure 5. 5). Previous polarised Raman experiments demonstrated that two Raman peaks around 180 cm<sup>-1</sup> were related to the Néel vector orientation [Ref. 5.14]. The Raman signal at 178 cm<sup>-1</sup> indicated the maximum intensity when the incident and output photon polarisation was parallel to the Néel vector. The resonant Raman shift energy changed from 178 to 180 cm<sup>-1</sup> in the cross-configuration, where the polarisation of the output photons was perpendicular to that of the input photons. The intensities at 178 and 180 cm<sup>-1</sup> showed a four-fold rotational symmetry, thus suggesting two candidates for the Néel vector orientation. We assumed that the Néel vector was parallel to the *a*-axis in the ground state

at a sufficiently low temperature to determine the  $a$ -axis. We also measured the polarised Raman spectra of the thermal cycles to test this assumption. First, we took the Raman spectra at 3 K, heated the sample to RT, and then collected the signals at 80 and 3 K upon cooling. The results obtained at different temperatures were consistent. The hexagonal structure of NiPS<sub>3</sub> shown in the OM images suggests three candidates for the  $a$ -axis [Ref. 5.15]. We determined the crystalline  $a$ -axis, consistent with the polarised Raman spectra and the morphology shown in the OM images.

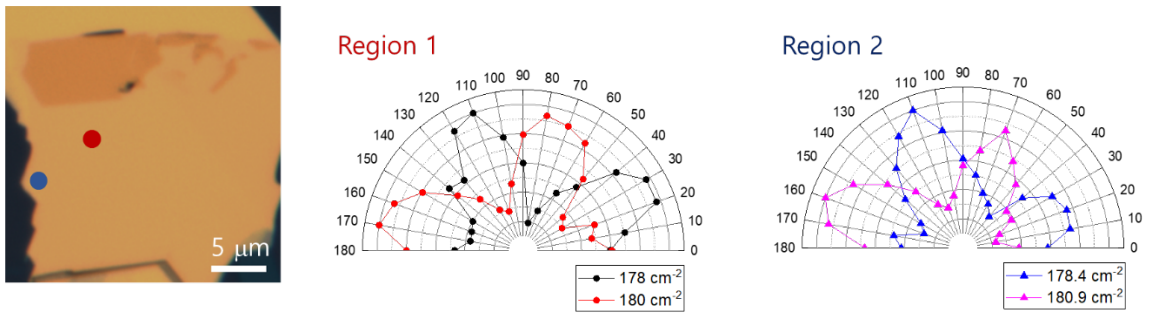


**Figure 5. 5 Polarisation-dependent Raman experiment for determining in-plane crystalline axis.** The red and blue circles on the OM image indicate the region of interest, notated as regions 1 and 2, respectively. Polarised Raman data are the results obtained at 3 K.

### 5.3.3 Determination of Néel vector axis

We extracted the X-ray absorption (XA) spectra from successive X-PEEM images as a function of photon energy. Figure 5. 6 shows the experimental XA spectra recorded at 70 and 285 K below and above  $T_N$ , respectively. The LD is defined as the intensity difference between two polarisations, i.e.  $I_{\parallel} - I_{\perp}$ . The LD below  $T_N$  was enhanced by the antiferromagnetic order from the XMLD effect. The remaining weak dichroic signal in the

paramagnetic state originated from a nonmagnetic contribution owing to the low symmetry of the trigonally distorted NiS<sub>6</sub> octahedron in NiPS<sub>3</sub> at all temperatures. The small short-range magnetic order also contributed to the non-zero dichroic signal. We verified the origin of the temperature-dependent LD using ligand field multiplet calculations. The trigonal symmetry  $D_{3d}$  at all temperatures and long-range magnetic orders below  $T_N$  were included in the calculations. The short-range magnetic order effect was reflected in other free parameters. As shown at the bottom of Figure 5. 6, the calculated spectra reproduced the experimental spectra well.

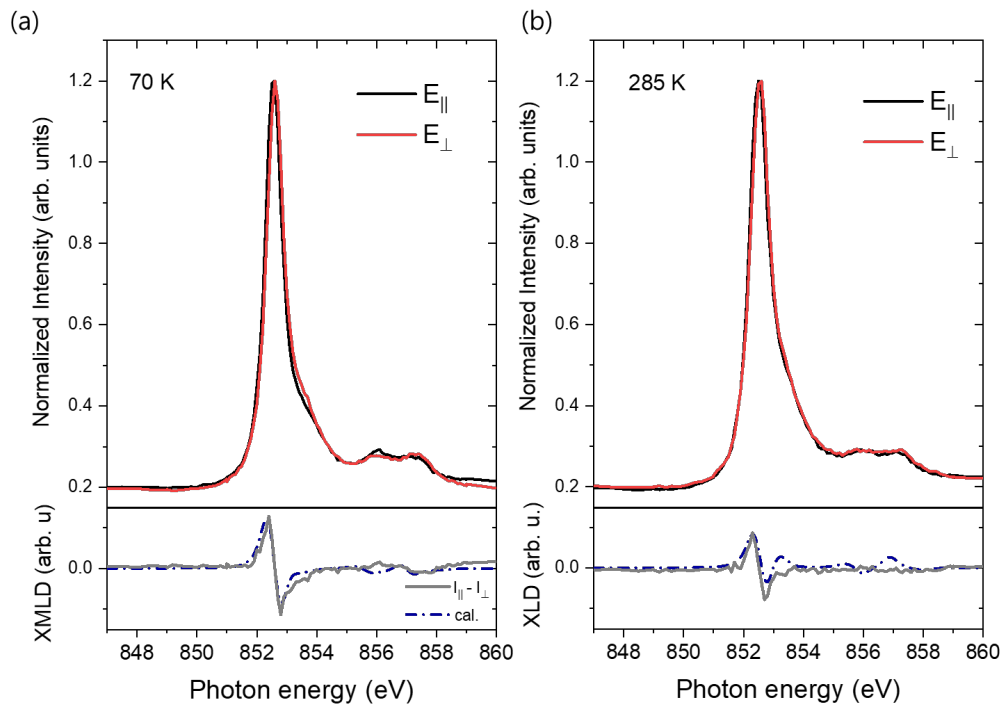


**Figure 5. 6 XA and X(M)LD spectra at Ni  $L_3$  edge.** Experimental XA spectra were captured at (a) 70 K ( $T < T_N$ ) and (b) 285 K ( $T > T_N$ ). Experimental (solid grey line) and calculated (dotted blue line) X(M)LD spectra are plotted at the bottom.

Hamiltonian	Parameters
Atomic terms $H_d$	60 % $F_{dd}$ , 70 % $F_{pd}$ , and 80 % $G_{pd}$ of atomic Hartree–Fock values $U_{dd} = 5.0$ eV $U_{pd} = 5.5$ eV $\xi_{3d} = 0.0826$ $\xi_{2p} = 11.5084$
Crystal field $H_c$	$10Dq = 0.6$ eV $D_{t2g} = 0.03$ eV
Ligand-metal charge transfer $H_{lmet}$	$\Delta = 0.95$ eV [Ref. 5.9] $\Delta' = -0.25$ eV $V_{a1g} = 2.0$ eV $V_{eg\pi} = 0.3$ eV $V_{eg\sigma} = 1.5$ eV
Ligand crystal field $H_L$	$10Dq^{lig} = 1.0$ eV $D_{t2g}^{lig} = 0.01$ eV

**Table 5. 1. Summary of parameters for multiplet simulation.** Each parameter is described in Chapter 4. 4. 1.

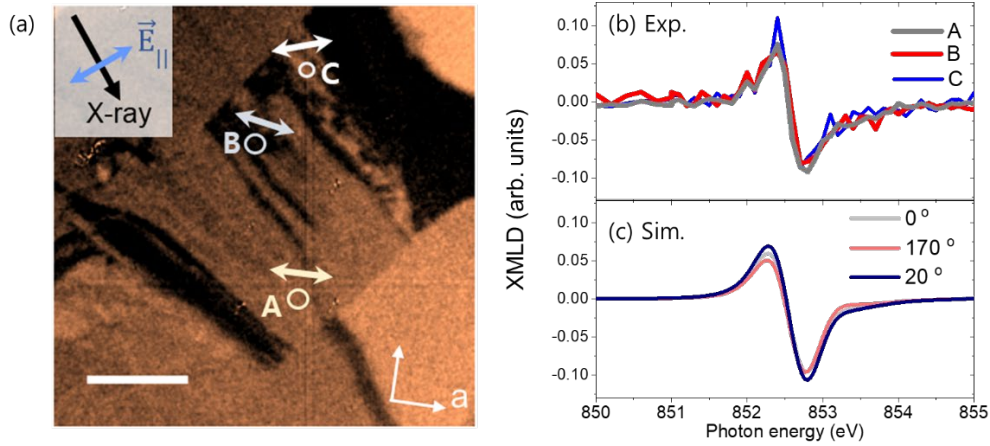


**Figure 5. 7 Determination of Néel vector axes in domains at 70 K.** (a) XMLD asymmetric image with calculated Néel vector axes of each domain (double arrows). The scale bar is 3  $\mu\text{m}$ . (b) Experimental XMLD spectra from domains A, B, and C. (c) Calculated XMLD spectra with different Néel vector axes. Legend indicates angles between Néel vector axes and crystalline  $a$ -axis.

The Néel vectors in each domain were determined via multiplet calculations of the XMLD spectra at 70 K. The other parameters were fixed, and the direction of the exchange field was rotated azimuthally to rotate the Néel vector axis. We selected three ROIs: domains A, B, and C (Figure 5. 7 (a)). The Néel vector in domain A was parallel to the  $a$ -axis. Meanwhile, the Néel vectors in domains B and C were rotated  $10^\circ$  (i.e.  $170^\circ$ ) and  $20^\circ$  from the  $a$ -axis, respectively (Figures 5. 7 (b–c)). The Néel vector orientations were irrelevant to the threefold rotational symmetry of monolayer NiPS<sub>3</sub>. The previously observed domains in FePS<sub>3</sub> and NiPS<sub>3</sub> exhibited three-fold rotational symmetry, which indicates that the three-fold rotation symmetry remained in the NiPS<sub>3</sub> and FePS<sub>3</sub> multilayers owing to weak interlayer vdW coupling [Ref. 5.4,5.6]. However, our domain structure did not exhibit the three-fold rotational symmetry but a multiplicity of more than three folds. This multiplicity in the direction of the Néel vectors was similarly observed in a magnetic field experiment

of NiPS<sub>3</sub> excitons [Ref. 5.10]. An external magnetic field was applied in the direction 120° from the *a*-axis. As the magnetic field increased, the Néel vector rotated continuously instead of at angles of three-fold symmetry, i.e. 60° and 120°.

### 5.3.4 Thermal fluctuation of magnetic domain

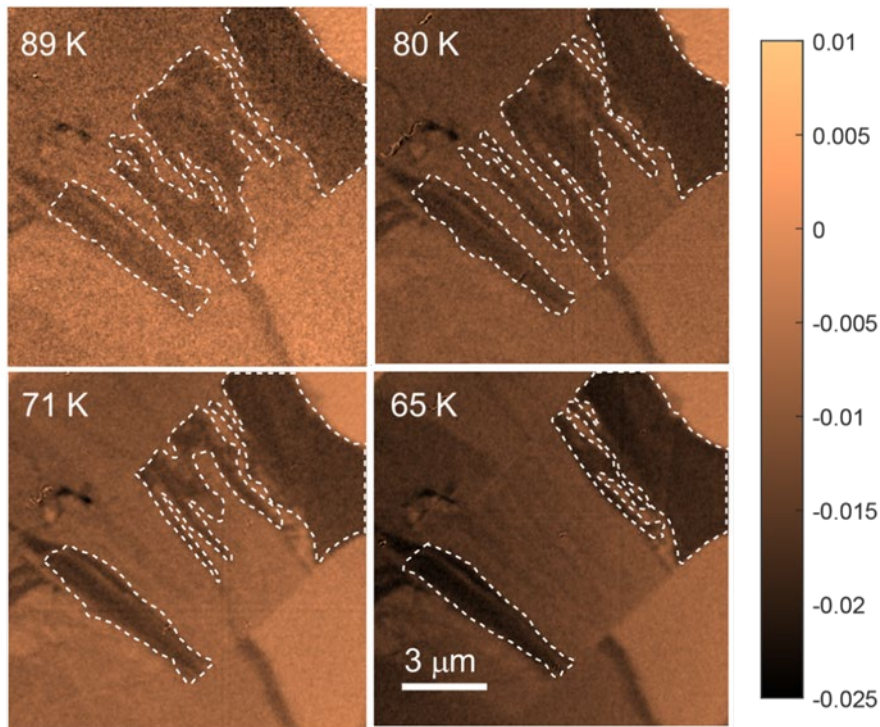


**Figure 5. 8 XMLD asymmetric images showing domains with thermal fluctuation.** The dashed white line provides visual guidance.

Thermal fluctuations were observed in the domains during cooling. As the temperature decreased, domains B and C merged into domain A, where the spins aligned along the *a*-axis (Figure 5. 8). This phenomenon indicated that the spins in NiPS<sub>3</sub> were not strongly pinned at 65 K. The thermally fluctuating domains excluded the structural origins of the

domains. The domains from the crystalline twin structure and the magnetoelastic effect from the substrate showed temperature-independent domain morphologies because the magnetostriction-induced strain hindered domain growth and fluctuations [Ref. 5.16,5.17]. The mobility of the local Néel vector demonstrated the high structural and chemical qualities of the NiPS<sub>3</sub> sample.

Weak magnetic anisotropy in NiPS<sub>3</sub> is the main mechanism contributing to the formation and thermal fluctuations of the magnetic domains. Spin wave analyses with neutron inelastic scattering experiments were performed, where a value of 0.01 meV was estimated for the easy-axis anisotropy along the *a*-axis [Ref. 5.18,5.19]. Based on the spin Hamiltonian, we successfully reproduced XMLD intensities in the magnetic domains using Monte Carlo (MC) simulations. The MC simulation used SU(N)NY, an open-source code for simulating general spin systems [Ref. 5.20]. The spin configuration of NiPS<sub>3</sub> was annealed from 200 to 70 K at temperature intervals of 0.95 K. At each temperature, and the spin configuration was thermalised using the Metropolis-adjusted Langevin algorithm over 2000-time steps. In the Metropolis-adjusted Langevin algorithm, we flipped the entire spin configuration at each time step using the Landau–Lifshitz–Gilbert equation of motion [Ref. 5.21]. We converted the spin configuration to the XMLD contrast map using the equation of XMLD intensity,  $I(\theta) = a + b(3\cos^2\theta - 1)\langle M^2 \rangle$ , where  $\theta$  is the angle between the incident x-ray *E*-polarisation and the spin axis [Ref. 5.13]. Figure 5.9 shows the reproduced XMLD map, which shows different local Néel vector orientations originating from the thermal excitation with low magnetic anisotropy.

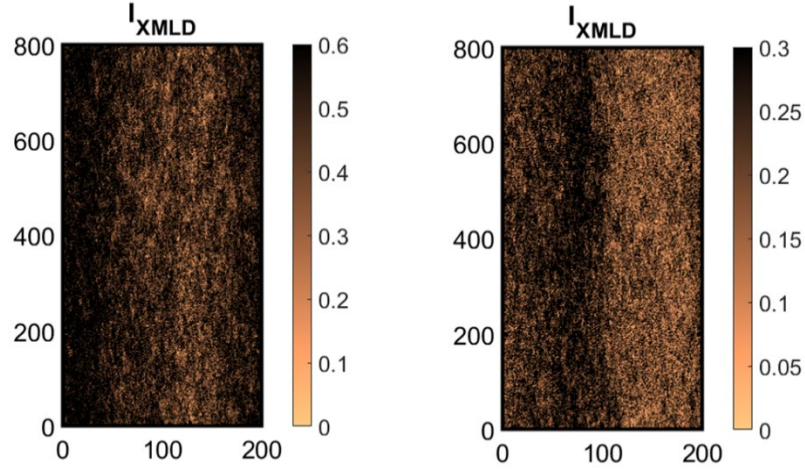


**Figure 5. 9 Reproduced XMLD map for magnetic domains in NiPS<sub>3</sub> via MC simulations.** The number shown on the x- and y- axes represent the number of spins along the axes. A total of 160,000 spins were simulated with four spins per unit cell in the  $C 2/m$  space group. The corresponding spatial dimension is approximately  $100 \text{ nm} \times 200 \text{ nm}$ .

The quenched orbital moment resulted in weak magnetic anisotropy. Multiplet simulations of the XA spectra showed that the in-plane orbital moments were  $L_a = 0.3667 \mu_B/Ni$  and  $L_b = 0.3666 \mu_B/Ni$ . We evaluated the magnetocrystalline energy using multiplet calculations and Bruno's theory [Ref. 5.22,5.23]. Based on the in-plane magnetic anisotropy, the energy difference between the energies of the spins parallel to the  $a$ - and  $b$ -axes, i.e.  $E_a - E_b$ , was  $-0.002 \text{ meV}$ . This value is similar to that based on the easy-axis anisotropy, i.e.  $-0.010 \pm 0.005 \text{ meV}$ , obtained from the neutron scattering experiment [Ref. 5.18].

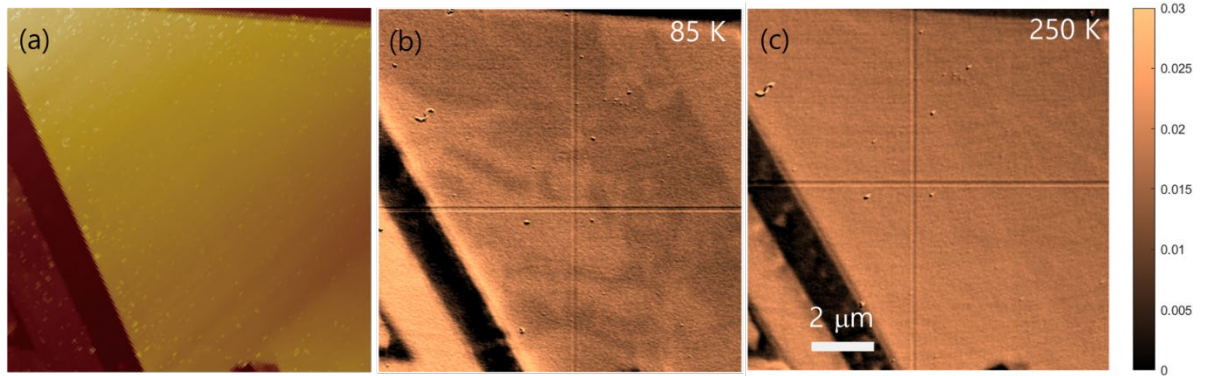


**Figure 5. 10 Antiferromagnetic domains in another NiPS<sub>3</sub> flake.** (a) AFM image of 87-nm-thick NiPS<sub>3</sub> flake. Corresponding asymmetric XMLD images at (b) 85 K (antiferromagnetic state) and (c) 250 K (paramagnetic state).

Next, we observed the magnetic domains in another NiPS<sub>3</sub> flake (Figure 5. 10). The observed domains similarly indicated a temperature-dependent domain contrast, thus confirming the magnetic origin of the domains. Finally, we investigated four NiPS<sub>3</sub> flakes using XPEEM and discovered a multidomain in two flakes.

## 5.4 Summary

In this study, we observed magnetic domains with different Néel vector orientations using XMLD-PEEM. The high-resolution X-ray imaging technique enabled the nano-meter scale domain in NiPS<sub>3</sub> to be imaged in real space and time, and the XMLD effect enabled direct access to local Néel vectors. The XMLD contrast of the temperature-dependent domains indicated their magnetic origins. In particular, changing the domain morphology at different temperatures demonstrated that the weak magnetic anisotropy of NiPS<sub>3</sub> induced the mobility of the Néel vectors. This study highlighted a probing technique for investigating vdW antiferromagnetic domains and the fundamental physics of magnetic anisotropy

associated with their formation and dynamics. Finally, studying local Néel vectors and their domains will provide helpful information for further developing NiPS<sub>3</sub> magneto-optical exciton-based devices.

## References

- [Ref. 5.1] Wittmann, A., Gomonay, O., Litzius, K., Kaczmarek, A., Kossak, A. E., Wolf, D., Lubk, A., Johnson, T. N., Tremsina, E. A., and Churikova, A. *Physical Review B* **106**, 224419, (2022).
- [Ref. 5.2] Ni, Z., Haglund, A. V., Wang, H., Xu, B., Bernhard, C., Mandrus, D. G., Qian, X., Mele, E. J., Kane, C. L., and Wu, L. *Nature Nanotechnology* **16**, 782-787, (2021).
- [Ref. 5.3] Ni, Z., Zhang, H., Hopper, D. A., Haglund, A. V., Huang, N., Jariwala, D., Bassett, L. C., Mandrus, D. G., Mele, E. J., and Kane, C. L. *Physical review letters* **127**, 187201, (2021).
- [Ref. 5.4] Ni, Z., Huang, N., Haglund, A. V., Mandrus, D. G., and Wu, L. *Nano Letters* **22**, 3283-3288, (2022).
- [Ref. 5.5] Zhang, Q., Hwangbo, K., Wang, C., Jiang, Q., Chu, J.-H., Wen, H., Xiao, D., and Xu, X. *Nano Letters* **21**, 6938-6945, (2021).
- [Ref. 5.6] Kim, D. S., Huang, D., Guo, C., Li, K., Rocca, D., Gao, F. Y., Choe, J., Lujan, D., Wu, T. H., and Lin, K. H. *Advanced Materials*, 2206585, (2023).
- [Ref. 5.7] Joy, P. A. and Vasudevan, S. *Phys. Rev. B* **46**, 5425-5433, (1992).
- [Ref. 5.8] Lançon, D., Ewings, R., Guidi, T., Formisano, F., and Wildes, A. *Physical Review B* **98**, 134414, (2018).
- [Ref. 5.9] Kang, S., Kim, K., Kim, B. H., Kim, J., Sim, K. I., Lee, J.-U., Lee, S., Park, K., Yun, S., and Kim, T. *Nature* **583**, 785-789, (2020).

- [Ref. 5.10] Wang, X., Cao, J., Lu, Z., Cohen, A., Kitadai, H., Li, T., Tan, Q., Wilson, M., Lui, C. H., and Smirnov, D. *Nature Materials* **20**, 964-970, (2021).
- [Ref. 5.11] Hwangbo, K., Zhang, Q., Jiang, Q., Wang, Y., Fonseca, J., Wang, C., Diederich, G. M., Gamelin, D. R., Xiao, D., and Chu, J.-H. *Nature Nanotechnology* **16**, 655-660, (2021).
- [Ref. 5.12] Sass, P. M., Ge, W., Yan, J., Obeysekera, D., Yang, J., and Wu, W. *Nano Letters* **20**, 2609-2614, (2020).
- [Ref. 5.13] Stöhr, J., Scholl, A., Regan, T., Anders, S., Lüning, J., Scheinfein, M., Padmore, H., and White, R. *Physical review letters* **83**, 1862, (1999).
- [Ref. 5.14] Kim, K., Lim, S. Y., Lee, J. U., Lee, S., Kim, T. Y., Park, K., Jeon, G. S., Park, C. H., Park, J. G., and Cheong, H. *Nat. Commun.* **10**, 345, (2019).
- [Ref. 5.15] Kuo, C.-T., Neumann, M., Balamurugan, K., Park, H. J., Kang, S., Shiu, H. W., Kang, J. H., Hong, B. H., Han, M., and Noh, T. W. *Scientific reports* **6**, 1-10, (2016).
- [Ref. 5.16] Scholl, A., Stöhr, J., Lüning, J., Seo, J. W., Fompeyrine, J., Siegwart, H., Locquet, J.-P., Nolting, F., Anders, S., and Fullerton, E. *Science* **287**, 1014-1016, (2000).
- [Ref. 5.17] Xu, J., Zhou, C., Jia, M., Shi, D., Liu, C., Chen, H., Chen, G., Zhang, G., Liang, Y., and Li, J. *Phys. Rev. B* **100**, 134413, (2019).
- [Ref. 5.18] Scheie, A., Park, P., Villanova, J., Granroth, G., Sarkis, C., Zhang, H., Stone, M., Park, J.-G., Okamoto, S., and Berlijn, T. *arXiv preprint arXiv:2302.07242*, (2023).
- [Ref. 5.19] Wildes, A., Stewart, J., Le, M., Ewings, R., Rule, K., Deng, G., and Anand, K. *Phys. Rev. B* **106**, 174422, (2022).
- [Ref. 5.20] SU(N)NY program (<https://github.com/SunnySuite/Sunny.jl>).
- [Ref. 5.21] Dahlbom, D., Miles, C., Zhang, H., Batista, C. D., and Barros, K. *Physical Review B* **106**, 235154, (2022).
- [Ref. 5.22] Bruno, P. *PhD thesis, Université Paris Sud-Paris XI*, (1989).
- [Ref. 5.23] van der Laan, G. *Journal of Physics: Condensed Matter* **10**, 3239, (1998).

## **Chapter 6. Summary and outlook**

### **6.1. Summary**

We investigated the magnetic properties of the van der Waals antiferromagnets FePS<sub>3</sub> and NiPS<sub>3</sub> using the XMLD–PEEM technique. The sensitivity to antiferromagnetic order and high spatial resolution of XMLD–PEEM enables the magnetic probing of exfoliated samples. Theoretical analysis of the X-ray absorption and XMLD spectra provides direct access to the orbital and spin moments, enabling a comprehensive understanding of the magnetism in FePS<sub>3</sub> and NiPS<sub>3</sub>.

The all-encompassing keyword used in this study is magnetic anisotropy. The large magnetic anisotropy in FePS<sub>3</sub> protects the long-range antiferromagnetic order in the monolayer. This large magnetic anisotropy originates from the unquenched orbital moment owing to the low symmetry of FeS<sub>6</sub> and the spin–orbit coupling. The small magnetic anisotropy in NiPS<sub>3</sub> results in thermally fluctuating antiferromagnetic domains. In contrast to FePS<sub>3</sub>, the quenched orbital moment in NiPS<sub>3</sub> leads to a small magnetic anisotropy, inducing unpinned local Néel vectors.

### **6.2. Outlook**

The magnetic properties of pristine van der Waals antiferromagnets have been extensively studied over the past few years, including this work with PEEM. Research on van der Waals

magnets has also expanded to include heterostructures and moiré structures beyond a single component. We expect XMLD-PEEM to be an excellent technique for studying artificial structures.

The feasibility of using X-PEEM to study van der Waals heterostructures has been demonstrated for FM/AFM heterostructures composed of epitaxial films [Ref. 6.1]. Different chemical atoms have different resonance energies in X-ray absorption, which enables the selective probe. Owing to the element-selective detection, we can investigate the magnetic properties of each layer independently.

Twisted bilayer graphene hosts several strongly correlated states [Ref. 6.2]. Since the superconducting state was demonstrated in twisted graphene with a magic angle [Ref. 6.3, 6.4], numerous experiments have been performed on twisted graphene and transition metal dichalcogenides (TMDCs) [Ref. 6.5]. Compared to the active research on moiré structures in graphene and TMDCs, studies on magnetic moiré structures have been relatively rare. For example, moiré van der Waals magnets exhibit magnetic textures in real space [Ref. 6.6, 6.7]. Thus, a high spatial resolution and sufficient magnetic sensitivity are essential for studying moiré magnets. X-PEEM with polarised X-rays satisfies these criteria. We demonstrated the capability of successively probing the antiferromagnetic order on the FePS<sub>3</sub> monolayer and capturing local Néel vectors in NiPS<sub>3</sub> domains. We believe that X-PEEM is one solution to the research gaps in vdW magnet moiré physics.

## References

- [Ref. 6.1] Ohldag, H., Scholl, A., Nolting, F., Anders, S., Hillebrecht, F. U., and Stöhr, J. *Physical Review Letters* **86**, 2878–2881, (2001).
- [Ref. 6.2] Andrei, E. Y. and MacDonald, A. H. *Nature Materials* **19**, 1265–1275, (2020).
- [Ref. 6.3] Cao, Y., Fatemi, V., Demir, A., Fang, S., Tomarken, S. L., Luo, J. Y., Sanchez–Yamagishi, J. D., Watanabe, K., Taniguchi, T., and Kaxiras, E. *Nature* **556**, 80–84, (2018).
- [Ref. 6.4] Cao, Y., Fatemi, V., Fang, S., Watanabe, K., Taniguchi, T., Kaxiras, E., and Jarillo–Herrero, P. *Nature* **556**, 43–50, (2018).
- [Ref. 6.5] Mak, K. F. and Shan, J. *Nature Nanotechnology* **17**, 686–695, (2022).
- [Ref. 6.6] Wang, C., Gao, Y., Lv, H., Xu, X., and Xiao, D. *Physical Review Letters* **125**, 247201, (2020).
- [Ref. 6.7] Song, T., Sun, Q.–C., Anderson, E., Wang, C., Qian, J., Taniguchi, T., Watanabe, K., McGuire, M. A., Stöhr, R., and Xiao, D. *Science* **374**, 1140–1144, (2021).
- [Ref. 6.1] Ohldag, H., Scholl, A., Nolting, F., Anders, S., Hillebrecht, F. U., and Stöhr, J. *Physical review letters* **86**, 2878-2881, (2001).
- [Ref. 6.2] Andrei, E. Y. and MacDonald, A. H. *Nature Materials* **19**, 1265-1275, (2020).
- [Ref. 6.3] Cao, Y., Fatemi, V., Demir, A., Fang, S., Tomarken, S. L., Luo, J. Y., Sanchez-Yamagishi, J. D., Watanabe, K., Taniguchi, T. ,and Kaxiras, E. *Nature* **556**, 80-84, (2018).
- [Ref. 6.4] Cao, Y., Fatemi, V., Fang, S., Watanabe, K., Taniguchi, T., Kaxiras, E. ,and Jarillo-Herrero, P. *Nature* **556**, 43-50, (2018).
- [Ref. 6.5] Mak, K. F. and Shan, J. *Nature Nanotechnology* **17**, 686-695, (2022).
- [Ref. 6.6] Wang, C., Gao, Y., Lv, H., Xu, X. ,and Xiao, D. *Physical review letters* **125**, 247201,

(2020).

[Ref. 6.7] Song, T., Sun, Q.-C., Anderson, E., Wang, C., Qian, J., Taniguchi, T., Watanabe, K.,  
McGuire, M. A., Stöhr, R. ,and Xiao, D. *Science* **374**, 1140-1144, (2021).

## Publication lists

- [1] Youjin Lee\*, Suhan Son\*, Chaebin Kim\* (equal contribution), Soonmin Kang, Junying Shen, Michel Kenzelmann, Bernard Delley, Tatiana Savchenko, Sergii Parchenko, Woongki Na, Ki-Young Choi, Wondong Kim, Hyeonsik Cheong, Peter M Derlet, Armin Kleibert, and Je-Geun Park, “Giant Magnetic Anisotropy in the Atomically Thin van der Waals Antiferromagnet FePS<sub>3</sub>”, *Adv. Electron. Mater.*, **9**, 2200650, (2023)
- [2] Youjin Lee, Chaebin Kim, Suhan Son, Jingyuan Cui, Giung Park, Kaixuan Zhang, Siwon Oh, Hyeonsik Cheong, Armin Kleibert, and Je-Geun Park, “Real space imaging of domain and dynamics in van der Waals antiferromagnet NiPS<sub>3</sub>” *in-preparation*
- [3] Hwiin Ju\*, Youjin Lee\* (equal contribution), Kwang-Tak Kim, In Hyeok Choi, Chang Jae Roh, Suhan Son, Pyeongjae Park, Jae Ha Kim, Taek Sun Jung, Jae Hoon Kim, Kee Hoon Kim, Je-Geun Park, and Jong Seok Lee, “Possible Persistence of Multiferroic Order down to Bilayer Limit of van der Waals Material NiI<sub>2</sub>”, *Nano Lett.*, **21**, 5126, (2021)
- [4] Suhan Son\*, Youjin Lee\*, Jae Ha Kim\*, Beom Hyun Kim\* (equal contribution), Chaebin Kim, Woongki Na, Hwiin Ju, Sudong Park, Abhishek Nag, Ke-Jin Zhou, Young-Woo Son, Hyeongdo Kim, Woo-Suk Noh, Jae-Hoon Park, Jong Seok Lee, Hyeonsik Cheong, Jae Hoon Kim, and Je-Geun Park, “Multiferroic-Enabled Magnetic-Excitons in 2D Quantum-Entangled Van der Waals Antiferromagnet NiI<sub>2</sub>”, *Adv. Mat.*, **34**, 2109144, (2022)
- [5] Youjin Lee\*, Dasom Kim\* (equal contribution), Jeeyoon Jeong, Jugyoung Kim, Volodymyr Shmid, Oleg Korotchenkov, Parinda Vasa, Young-Mi Bahk, and Dai-Sik Kim,

“Enhanced terahertz conductivity in ultra-thin gold film deposited onto (3-mercaptopropyl) trimethoxysilane (MPTMS)-coated Si substrates”, *Sci. Rep.*, **9**, 15025, (2019)

[6] Jangwon Kim\*, Youjin Lee\*, Young Woo Choi\* (equal contribution), Taek Sun Jung, Suhan Son, Jonghyeon Kim, Hyoung Joon Choi, Je-Geun Park, and Jae Hoon Kim, “Terahertz Spectroscopy and DFT Analysis of Phonon Dynamics of the Layered Van der Waals Semiconductor Nb<sub>3</sub>X<sub>8</sub> (X = Cl, I)”, *ACS Omega*, **8**, 14, (2023)

[7] Kiin Nam\*, Youjin Lee\* (equal contribution), SeongYeon Kim, Sunghwan Kim, Sung Ju Hong, Wonjong Choi, Jinhee Lee, Hyelin Kim, Dai-Sik Kim, JunHo Kim, Soobong Choi, and Young-Mi Bahk, “Copper-based etalon filter using antioxidant graphene layer”, *Nanotechnol.* **31**, 445206, (2020)

[8] Kaixuan Zhang, Seungyun Han, Youjin Lee, Matthew J Coak, Junghyun Kim, Inho Hwang, Suhan Son, Jeacheol Shin, Mijin Lim, Daegeun Jo, Kyoo Kim, Dohun Kim, Hyun-Woo Lee, and Je-Geun Park, “Gigantic Current Control of Coercive Field and Magnetic Memory Based on Nanometer-Thin Ferromagnetic van der Waals Fe<sub>3</sub>GeTe<sub>2</sub>” *Adv. Mat.*, **33**, 2004110, (2021)

[9] Kaixuan Zhang, Youjin Lee, Matthew J Coak, Junghyun Kim, Suhan Son, Inho Hwang, Dong-Su Ko, Youngtek Oh, Insu Jeon, Dohun Kim, Changgan Zeng, Hyun-Woo Lee, and Je-Geun Park, “Highly Efficient Nonvolatile Magnetization Switching and Multi-Level States by Current in Single Van der Waals Topological Ferromagnet Fe<sub>3</sub>GeTe<sub>2</sub>”, *Adv. Funct. Mat.*, **31**, 2105992, (2021)

[10] Junghyun Kim, Suhan Son, Matthew J Coak, Inho Hwang, Youjin Lee, Kaixuan Zhang, and Je-Geun Park, “Observation of plateau-like magnetoresistance in twisted Fe<sub>3</sub>GeTe<sub>2</sub>/Fe<sub>3</sub>GeTe<sub>2</sub> junction”, *J. Appl. Phys.*, **128**, 093901 (2020)

- [11] Sunghwan Kim, Dasom Kim, Youjin Lee, Geon Lee, Jeeyoon Jeong, Dukhyung Lee, and Dai-Sik Kim, “Broadband high-performance terahertz polarizer based on a dense array of 5 nm gap slit antennas”, *Opt. Express.*, **30(17)**, 30038, (2022)
- [12] Woongkyu Park, Youjin Lee, Taehee Kang, Jeeyoon Jeong, and Dai-Sik Kim, “Terahertz-driven polymerization of resists in nanoantennas”, *Sci. Rep.*, **8**, 1 (2018)
- [13] Jiyeah Rhie, Dukhyung Lee, Young-Mi Bahk, Jeeyoon Jeong, Geunchang Choi, Youjin Lee, Sunghwan Kim, Seunghun Hong, and Dai-Sik Kim, “Control of optical nanometer gap shapes made via standard lithography using atomic layer deposition”, *J. Micro/Nanolith. MEMS MOEMS*, **17**, 023504 (2018)
- [14] Geunchang Choi, Young-Mi Bahk, Taehee Kang, Youjin Lee, Byung Hee Son, Yeong Hwan Ahn, Minah Seo, and Dai-Sik Kim, “Terahertz nanoprobng of semiconductor surface dynamics”, *Nano. Lett.*, **17**, 6395 (2017)

국문초록

엑스선 광전자 현미경을 이용한  
반데르발스 반강자성체의 자성 연구

이유진

물리천문학부 물리학전공

서울대학교 대학원

2004년에 발표된 흑연으로부터 스카치 테이프를 이용한 그래핀 박리 기술은 응집 물리 분야의 새로운 국면을 열었다. 이러한 기념비적인 시연을 시작으로 이차원 반데르발스 물질에 대한 많은 연구가 뒤따랐고, 마침내 2016년에 최초로 이차원 반강자성 단일층이 실험적으로 증명되었다. 이차원 반데르발스 자성체는 이차원 자성을 연구하기에 이상적인 물질로, 반데르발스 자성체마다 다른 스핀 해밀토니안 모델은 이차원 자기 이론을 실험적으로 검증할 수 있는 시험대를 제공한다. 또한 최근의 이차원 반데르발스 자성체의 연구는 단순히 반데르발스 자성체 본 물질의 고유 자기 특성 탐구를 넘어 이중 구조 및 모아레 구조까지 확장하고 있다.

이와 같이 이차원 반데르발스 자성체의 연구가 빠르게 확장하면서, 정밀한 측정 기술은 연구에 핵심 요소가 되었다. 그러나 이차원 자성체의 물리적 중요성과 전도유망한 응용력에도 불구하고 매우 얇은 반데르발스 자성체의 자기 상태, 특히 반강자성체의 자기 상태를 측정하는 것은 여전히 어려운

과제로 남아있다. 박리된 얇은 반데르발스 자성체의 초소형 부피와 이로 인한 작은 자기 신호는 자성 측정의 주요 장애물이며, 특히 반강자성체의 영에 가까운 순 자화 신호는 추가적인 어려움을 야기한다.

본 연구에서는 측정 기술을 확장하고, 이차원의 극한에서 발생하는 현상을 관측하기 위해 이차원 반데르발스 반강자성체의 연구에 엑스선 광전자 현미경을 적용하였다. 선형 편광의 엑스선을 이용하여 쌍극자 선택 규칙에 의해 발생하는 엑스선 자기 선형 이색성 효과를 통해 반강자성의 자기 상태를 측정할 수 있었다. 또한 엑스선 광전자 현미경의 높은 공간 분해능을 통해 가로 길이가 수 마이크로미터 수준의 박리된 반데르발스 반강자성체를 측정할 수 있었다.

본 연구에서는 특히 두 가지 유형의 스핀 해밀토니안을 갖는 반데르발스 반강자성체, Ising 유형의  $\text{FePS}_3$ 와 anisotropic Heisenberg 유형의  $\text{NiPS}_3$ 의 자기 특성을 조사하는 데 중점을 두었다. 엑스선 광전자 현미경을 이용하여 1960년대에 이론물리학자 Onsager가 이론적으로 예측한 바와 같이 Ising 유형의  $\text{FePS}_3$  단일층에서 반강자성 자기 상전이가 존재한다는 것을 확인하였다. 또한 관측한 엑스선 흡수 스펙트럼을 분석하고 multiplet 계산을 통해  $\text{FePS}_3$ 의 자기 이방성을 두께에 따라 정량화 할 수 있었다. 벌크  $\text{FePS}_3$ 는 유한한 오비탈 모멘트와 스핀-오비탈 결합을 통해 큰 자기 이방성을 가지고 있었다. 또한, 두께에 따른 자기 이방성은 반데르발스 물질의 연구에서 흔히 간과되는 기판 효과에 대한 통찰력을 제공하였다. 박리된  $\text{NiPS}_3$ 에서는 반강자성 도메인을 관측하였다. 도메인의 열적 변동을 통해 해당 물질의 유동적인 닐 벡터 (Néel vector)를 확인할 수 있었다. 또한

NiPS<sub>3</sub>의 작은 자기 이방성으로 인해 도메인이 형성되며 도메인이 열적 변동을 보인다는 것을 알아냈다.

**주요어:** 이차원 반데르발스 자성체, 반강자성, 엑스선 광전자 현미경, 엑스선 자기 선형 이색성

**학 번:** 2016-20314

## **Acknowledgement (감사의 글)**

I would like to express my deep gratitude to my supervisor, professor Je-Geun Park, for his great support and guidance throughout my Ph. D. journey. He gave me the chance to change my research field. With his tolerance and generosity, I could settle on a new group and research area. He has disciplined me to be an independent and self-motivated scientist and a good collaborator with other scientists. I am also grateful to my thesis committee members Prof. Kee Hoon Kim, Hongki Min, Dohun Kim and Dr. Armin Kleibert, for their helpful feedback and advice for this thesis.

Dr. Armin was not only my thesis committee member but a supervisor of my X-PEEM project as a beamline scientist of SIM beamline, Swiss Light Source. He supported the whole process of X-PEEM experiments from the sample preparation to the analysis and write the paper. I could be skilled in performing X-PEEM experiments with his help. I also learned a great deal from his sharp and critical intuition and analysis of scientific problems. I also appreciated the collaborators at Paul Scherrer Institute. Dr. Peter. M. Derlet provided the nice Monte-Carlo simulation and Prof. Michel Kenzelmann shared the discussion on FePS<sub>3</sub> X-PEEM result. Dr. Junying Shen participated in FePS<sub>3</sub> X-PEEM experiments. I have to be grateful to other collaborators on the X-PEEM project. Prof. Hyeonsik Cheong, Dr. Woongki Na and Siwon Oh performed the Raman experiments on the sample to support my X-PEEM experiments results. Dr. Wondong Kim helped me carry out the multiplet

calculations with helpful comments.

I would thank all our EPG members for their sincere help and encouragement. Without their support, I could not finish my Ph. D. course. My colleagues, Dr. Soonmin Kang, Dr. Suhan Son, Dr. Kaixuan Zhang, Gi-Ung Park, Jingyuan Cui, and Hyuncheol Kim engaged in the X-PEEM experiments. They helped me prepare samples, perform experiments, and discuss data. Especially Dr. Suhan laid the foundation of X-PEEM experiments before my projects and figured out the important key parameter in FePS<sub>3</sub> X-PEEM results. His efforts in successive experiments to optimize experimental conditions resulted in the success of subsequent experiments. I also thank other vdW team members, Dr. Kaixuan Zhang, Inho Hwang, Junghyun Kim, Gi-Ung Park, Jingyuan Cui, Hyuncheol Kim and Jihoon Keum for being nice colleagues. It was my pleasure to discuss with them and learn their techniques and physical insight. The scattering/material team members, Dr. Kiso Park, Dr. Taehun Kim, Dr. Seokhwan Yun, Dr. Pyeongjae Park, Cheabin Kim, Heejun Yang, Yeochan An, and Woonghee Cho also shared brilliant ideas and constructive discussion. Chaebin Kim contributed to the theoretical part of my thesis. His excellent calculations on multiplet of FePS<sub>3</sub> and the simulation on NiPS<sub>3</sub> domains strengthened the logic of the argument. And I acknowledged the support from Erika Beard, Youngeun Shin, and Dr. Janae Park.

I also appreciated Prof. Dai-sik Kim, my supervisor for the first three years of the integrated Ph. D course. He emphasized the passion, and the importance of wrap-up of the project. I am grateful to members of the nano-optics group. Prof. Dr. Young-mi Bahk supervised my Bachelor's thesis and my two journal papers including the first paper of mine.

## *Acknowledgement*

---

She kindly taught me the experimental techniques and background of THz plamonics step by step. And I also appreciated Dasom Kim, the co-first author of my first paper. He patiently guided the experiments and the manuscript. I sincerely appreciated Dr. Jiyeah Rhie, Dr. Taehee Kang, Prof. Dr. Geunchang Choi. They are great senior scientists with whom I could discuss the scientific problem and matters of daily life. With their warm encouragement, I could endure the troubles in my Ph. D. course.

마지막으로 제 정신적, 신체적 뿌리가 되어 주신 부모님과 조부모님께 감사의 인사를 드리고 싶습니다. 부모님의 정신적, 물질적 지원이 없었다면 여기까지 결코 올 수 없었을 것입니다. 무뚝뚝한 딸이기에 표현을 하진 않았지만, 연구자로서의 고민에 조언을 해주신 아버지께 늘 감사함과 존경심을 느끼고 있습니다. 저에게 친구이자, 언니이자, 어머니로서 조언과 공감을 아끼지 않으시는 어머니에게도 감사드립니다. 항상 사랑으로 감싸주신 조부모님에게도 감사의 인사를 드리고 싶습니다. 할머니, 할아버지의 보살핌으로 제가 여기까지 올 수 있었다는 걸 항상 기억하고 있습니다. 돌아가신 할아버지, 할머니에게도 감사드립니다. 여기에 다 적진 못했지만 제 연구 활동 및 연구생 생활을 도와주신 모든 분께 감사드리며 감사의 글을 마치도록 하겠습니다.